Detection and Tracking of Tropical Convective Storms Based on Globally Gridded Precipitation Measurements: Algorithm and Survey over the Tropics⌖

HANII TAKAHASHI,[a,b] MATTHEW LEBSOCK,[b] ZHENGZHAO JOHNNY LUO,[c] HIROHIKO MASUNAGA,[d] AND CINDY WANG[e]

[a] Joint Institute for Regional Earth System Science and Engineering, University of California, Los Angeles, California
[b] Jet Propulsion Laboratory, California Institute of Technology, Pasadena, California
[c] Department of Earth and Atmospheric Sciences, City University of New York, City College, New York
[d] Institute for Space-Earth Environmental Research, Nagoya University, Nagoya, Japan
[e] Program in Atmospheric and Oceanic Sciences, Princeton University, Princeton, New Jersey

ABSTRACT: This paper is the first attempt to document a simple convection-tracking method based on the IMERG precipitation product to generate an IMERG-based Convection Tracking (IMERG-CT) dataset. Up to now, precipitation datasets have been Eulerian accumulations. Now with IMERG-CT, we can estimate total rainfall based on Lagrangian accumulations, which is a very important step in diagnosing cloud-precipitation process following the evolution of air masses. Convection-tracking algorithms have traditionally been developed on the basis of brightness temperature (Tb) from satellite infrared (IR) retrievals. However, vigorous rainfall can be produced by warm-topped systems in a moist environment; this situation cannot be captured by traditional IR-based tracking but is observed in IMERG-CT. Therefore, an advantage of IMERG-CT is its ability to include the previously missing information of shallow clouds that grow into convective storms, which provides us more-complete life cycle records of convective storms than traditional IR-based tracking does. This study also demonstrates the utility of IMERG-CT through investigating various properties of convective systems in terms of the evolution before and after peak precipitation rate and amount. For example, composite analysis reveals a link between evolution of precipitation and convective development: the signature of stratiform anvils remaining after the storm has produced the maximum rainfall, as average Tb stays almost constant for 5 h after the peak of precipitation. Our study highlights the importance of joint analysis of cloud and precipitation data in time sequence, which helps to elucidate the underlying dynamic processes producing tropical rainfall and its resultant effects on the atmospheric thermodynamics.

KEYWORDS: Tropics; Storm tracks; Precipitation; Cloud tracking/cloud motion winds; Databases; Microwave observations

1. Introduction

An attempt to understand the variability of precipitation life cycles was originally made nearly three decades ago using visible and infrared (IR) geostationary satellite imaging (Griffith et al. 1978). Since then, there has been a growing literature about convective evolutions and their associated precipitation life cycles based on analyses of convection-tracking methods using satellite IR retrievals.

Convection tracking was originally done manually (e.g., Martin and Schreiner 1981; Velasco and Fritsch 1987; Miller and Fritsch 1991; Laing and Fritsch 1993a,b; Rowell and Milford 1993). Although it revealed interesting aspects of convective evolution, such manual tracking was limited in its sample size and consistency because it was labor intensive and could be subjective. To overcome the limitations of manual tracking, Woodley et al. (1980) and Williams and Houze (1987)

proposed automatic tracking algorithms. Following these two pioneering studies, the literature based on automated convection tracking has grown. The classic way to identify and track deep convective systems is to use a cold brightness temperature (Tb) threshold from satellite IR images to define continuous areas of deep convective cloudiness. The selection of Tb varies from analysis to analysis, but usually ranges from 208 to 255 K (Fiolleau and Roca 2013a). Since this range of Tb corresponds to a range of altitudes greater than 5 km, the number of convective objects tracked, their extent, and lifetime are sensitive to the choice of Tb.

The tracking algorithms also vary from one study to another. The most popular algorithm has been the area overlapping technique that estimates the fraction of the geographical overlap between convective clouds on two successive images (Arnaud et al. 1992; Williams and Houze 1987). One of the most notable is Machado et al. (1998), which developed an algorithm using the International Satellite Cloud Climatology Project (ISCCP) Pixel Level Cloud Product (DX) datasets (Rossow and Schiffer 1999) to track the evolution of mesoscale convective systems through their life cycles. Such datasets are called ISCCP convection-tracking (CT) datasets. In the ISCCP-CT datasets, connected IR pixels with Tb < 245 K and with Tb < 220 K are identified as convective systems and convective clusters, respectively. The ISCCP-CT datasets

cover latitudes < 55° for more than 30 years, which gives us opportunities to study convective properties and features of mesoscale convective systems in different life stages (e.g., Takahashi and Luo 2014; Vant Hull et al. 2016).

While the existing approaches to tracking convective storms have resulted in a great deal of progress in our understanding of convective storms, their motivation is not always to monitor the evolution of precipitation per se, but to monitor the evolution of convective storms that are convecting and precipitating. There are fundamental limitations of using IR retrievals based on Tb thresholds for the purpose of tracking precipitation evolution. First, thinner in situ cirrus clouds (unassociated with active convection) are IR semitransparent and look warmer, and thus such clouds can be excluded when colder Tb thresholds are applied (Machado et al. 1998). However, some of thicker in situ cirrus clouds can be nearly as cold as convective storms and thus they can be incorrectly identified as deep convective systems. Second, even when cold Tbs are associated with convection, there is a poor correlation between Tb and precipitation rate (e.g., Karbalaee et al. 2017a,b). To monitor both cloud and precipitation evolution, which is our purpose of this study, we argue that these shortcomings can be mitigated if a tracking algorithm is applied to precipitation patterns instead of IR imagery.

Liu et al. (2008) compiled a precipitation feature database from measurements of radar and visible, IR, and microwave (MW) radiometers on the Tropical Rainfall Measuring Mission (TRMM; Kummerow et al. 1998) satellite. This TRMM-based cloud and precipitation feature database has been used to study the regional variations of rainfall characteristics, vertical structure of rainfall, convective properties, as well as diurnal variations of precipitation (e.g., Xu and Zipser 2011; Luo et al. 2013). However, TRMM, a low-Earth-orbiting satellite flying over a certain location several times per day, is limited in sampling frequency, which makes it difficult to monitor hourly scale variability critical to precipitation cycles. For this purpose, a gridded high-spatiotemporal-resolution precipitation product is required.

Such precipitation products exist. For example, the National Oceanic and Atmospheric Administration (NOAA) Climate Prediction Center morphing technique (CMORPH; Joyce et al. 2004) and TRMM 3B42 (Huffman et al. 2007) have a spatial resolution of 0.25° and a temporal resolution of 3 h, and the Global Satellite Mapping of Precipitation (GSMaP; Kubota et al. 2007; Ushio et al. 2009), one of the Global Precipitation Measurement (GPM; Hou et al. 2014) mission products like Integrated Multisatellite Retrievals for GPM (IMERG), has a spatial resolution of 0.1° and a temporal resolution of 1 h. Previous studies used them for a variety of research topics: regional model evaluations (e.g., Beucher et al. 2014; Zhang and Anagnostou 2019), physics of costal convection (Coppin et al. 2020), precipitation duration (White et al. 2017), diurnal cycles (Janowiak et al. 2005), and Madden–Julian oscillation (Kerns and Chen 2016, 2020). A previous study also made a comparison between gridded precipitation like 3B42 and IR based gridded data, which showed no improvements using gridded precipitation (Dias et al. 2017). However, many previous studies demonstrated that the approach

of merging IR and precipitation provided some insight into the life cycle of isolated tropical cold cloud systems (Imaoka and Nakamura 2012), tropical mesoscale convective systems (Fiolleau and Roca 2013a,b), midlatitude deep convective systems (Feng et al. 2012), and deep convective system (Futyan and Del Genio 2007). The present study further explores the utility of global precipitation datasets with focus on properties of the precipitation life cycle including systematic differences between cloud-top temperature and surface precipitation, which have not been well documented before.

Beginning in 2014, GPM released a new generation of the precipitation product IMERG (Huffman et al. 2020), which offers global precipitation monitoring with a spatial resolution of 0.1° and a temporal resolution of 0.5 h. This high-spatiotemporal-resolution precipitation product has not yet received a systematic validation at its full resolution although its regional errors and biases are well documented (e.g., Gosset et al. 2018; Anjum et al. 2018; Sharifi et al. 2019), and issues due to inhomogeneity in space and time also have been reported (e.g., Tan et al. 2019). Although there have been some limitations and uncertainties in IMERG (see section 5), the quality of IMERG has improved as the versions of IMERG have been constantly updated. The latest version, IMERG V06B, was released on June 2019, and a recent study of Tang et al. (2020) claims that the IMERG V06B outperforms many satellite precipitation products such as TRMM 3B42, CMORPH, PERSIANN-CDR (Ashouri et al. 2015), Climate Hazards Group Infrared Precipitation with Stations (CHIRPS; Funk et al. 2014), and Soil Moisture to Rain (SM2RAIN; Brocca et al. 2014). Taking advantage of this opportunity, we develop an algorithm to identify and track tropical convective storms based on the latest version of IMERG V06B.

The present paper is the first, to our knowledge, to use IMERG to conduct convection tracking. Therefore, the main purpose of this paper is to document a simple convection-tracking method based on the newly developed IMERG product to generate an IMERG-based convection-tracking dataset (IMERG-CT). It is worth pointing out that up to now precipitation datasets have been Eulerian accumulations. However, with IMERG-CT, it is now possible to estimate not only the time evolution of instantaneous rain intensity but also the lifetime-accumulated precipitation amount of each convective storm. Therefore, this precipitation-based convection-tracking algorithm provides the highest global spatiotemporal resolution of any algorithm to date that able to monitor precipitation evolution from the Lagrangian perspective.

Moreover, since we also include some information on cloud tops based on IR imagery in IMERG-CT, the link between the evolution of precipitation and convective cloud development can be examined. Thus, another purpose of this paper is to demonstrate the utility of IMERG-CT through investigating the linkage between precipitation and cloud properties such as Tb. Therefore, in addition to IMERG precipitation product, we use the latest ISCCP product, ISCCP H-series pixel-level global (HXG), to get information of Tb. Moreover, lidar and radar products based on *CloudSat* observations are used to evaluate the IMERG-CT algorithm. These satellite datasets

used in this study are described in the next section. Section 3 explains the algorithms of IMERG-CT. Some evaluations and sensitivity tests for IMERG-CT are conducted in section 4. Results based on statistical and composite analysis are presented in section 5, followed by section 6, where the key findings are summarized and discussed.

2. Data

a. IMERG

The IMERG product 3IMERGHH is used to estimate gridded surface precipitation. The horizontal and temporal resolutions of this latest IMERG product, 3IMERGHH, have been improved from 0.25° to 0.1° latitude/longitude spatial resolution (~10 km in the tropics), and from a 3-hourly to a 30-min temporal resolution. This offers global precipitation monitoring based on a merged retrieval using algorithms developed by several groups: TRMM Multisatellite Precipitation Analysis (TMPA; Huffman et al. 2007), Climate Prediction Center Morphing with Kalman Filter (CMORPH-KF; Joyce and Xie 2011), and microwave recalibrated PERSIANN-CCS (Hong et al. 2004). Basically, the algorithms intercalibrate and merge "all" satellite microwave rain estimators, together with MW-calibrated IR satellite estimators, precipitation gauge analyses, and combined radar–radiometer precipitation estimations where TRMM and GPM observations are available, at fine time and space scales over the whole globe. It is critical to note that although the IMERG data product uses infrared observations to fill in spatial and temporal gaps, the infrared is anchored to much more reliable precipitation estimates by microwave observations (both preceding and following the analysis time) wherever available. [Huffman et al. (2020) provides an overview of the IMERG product and the data are available at https://storm.pps.eosdis.nasa.gov/storm/.] In this study, we use "precipitaionCal," or multisatellite precipitation estimates with gauge calibration for precipitation rate.

b. CloudSat

CloudSat (http://www.cloudsat.cira.colostate.edu/) is a polar-orbiting satellite that overpasses the equator at ~0130/1330 local time. CloudSat carries a 94-GHz Cloud Profiling Radar (CPR), which has a horizontal resolution of 1.7 km along track by 1.4 km across track as well as a vertical resolution of 480 m oversampled at 240 m. CPR is sensitive to both cloud- and precipitation-size particles and has the capability of providing vertical structures of clouds. In this study, we use information about cloud layers from 2B–Geometrical Profiling Product (GEOPROF)-lidar, and the cloud mask and the calibrated radar reflectivity profiles from the 2B-GEOPROF product (Marchand et al. 2008). An overview of the CloudSat mission is summarized in Stephens et al. (2008).

c. ISCCP-HXG

Since 1982, ISCCP has provided global cloud information based on geostationary satellite data. A pixel-level cloud product called DX, whose temporal and spatial resolutions are limited to mesoscale (i.e., 30-km mapped pixel and a 3-h time interval), has been widely used, especially for conducting the ISCCP-CT dataset described in the introduction. In 2017, the new pixel-level cloud product called HXG was released, which has higher spatial sampling of ~10 km (0.1° latitude/longitude) when compared with DX. (ISCCP-HXG is available at https://www.ncdc.noaa.gov/isccp/isccp-data-access, which covers the period from 1982 to 2018.) Detailed information about the ISCCP-HXG cloud product is provided by Young et al. (2018).

d. Instantaneous comparison between IMERG and HXG

Although the heaviest rainfall is often assumed to be associated with the tallest convective towers, a previous study (Hamada et al. 2015) suggests that the linkage between intensity of rainfall and convective development remains weak since warm rain can be heavier than cold rain under a certain environment. It is also known that cirrus anvils can be as cold as convective cores, but they do not produce heavy rain like convective cores. Therefore, it is interesting to explore the link between cloud-top temperature (i.e., infrared brightness temperatures) from ISCCP-HXG and precipitation rate from IMERG. ISCCP-HXG has a lower temporal resolution (3 h) than IMERG (30 mins), yet ISCCP-HXG has the same spatial resolution as IMERG (0.1° latitude/longitude), which makes it easier to explore an instantaneous link between them. Figure 1 shows instantaneous comparisons between precipitation ($>0.01\,\mathrm{mm\,h^{-1}}$) and Tb with different thresholds, and as expected, correlations between Tb and precipitation ($>0.01\,\mathrm{mm\,h^{-1}}$) are low as shown in Table 1. This result indicates that IR imagery alone has difficulties in monitoring precipitation. IMERG and other precipitation products of similar design attempt to push this limit by incorporating satellite microwave measurements wherever available, although the accuracy of estimates is not always assured when the absence of microwave observations are filled in by infrared observations. This is a primary motivation to use IMERG precipitation rate rather than IR Tb to identify and track rain events. We further test if light rainfall (precipitation $> 0.5\,\mathrm{mm\,h^{-1}}$) and relatively heavy precipitation (precipitation $> 5\,\mathrm{mm\,h^{-1}}$) correlate better with some Tb, but spatial correlations get even lower (Table 1). It is very interesting to see that a decrease or increase of Tb thresholds does not change the correlations between precipitation rate and Tb by much. This result suggests that the evolution of rainfall intensity does not always follow that of cloud-top development and suggests that the peak of cloud top that reaches minimum Tb and the peak of rain event that reaches maximum precipitation do not necessarily happen simultaneously. Therefore, it is interesting to further explore the temporal separation between the two peaks to understand the life cycles of tropical convective storms, which is a central motivation for developing IMERG-CT.

3. Definition of tropical convective storm and tracking algorithm

Our primary focus is to track the evolution of precipitation in tropical convective storms. Therefore, we apply a tracking algorithm over IMERG by identifying precipitation cores
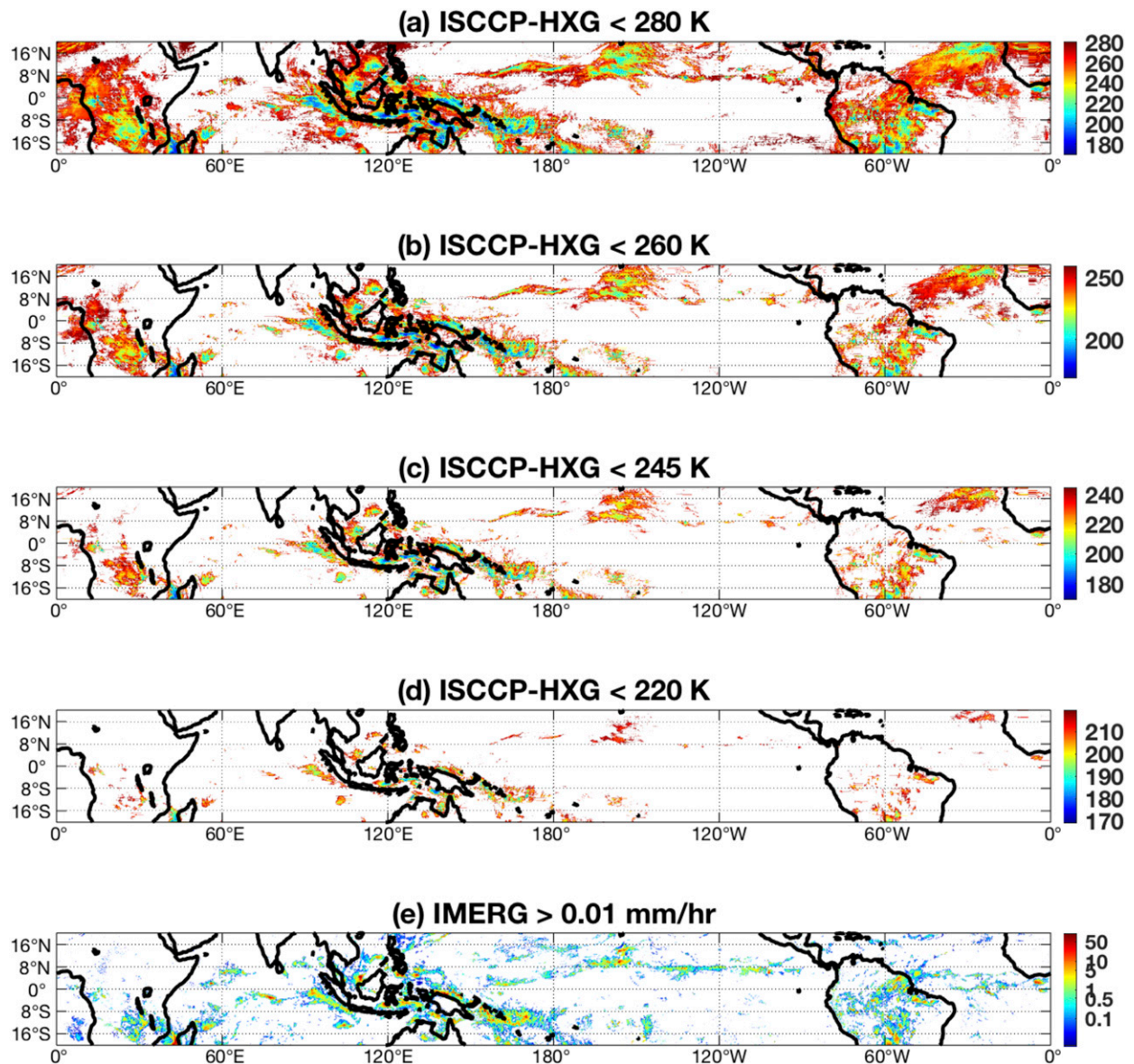
FIG. 1. Tropical maps of (a)–(d) Tb from ISCCP-HXG based on different thresholds as labeled and (e) precipitation rate ($>0.01 \, \mathrm{mm \, h^{-1}}$) from IMERG at 0000 UTC 1 Jan 2008.

(PCs) and precipitation systems (PSs) between 20°S and 20°N latitude.

a. Precipitation cores and precipitation systems

Similar to ISCCP-CT, we use two thresholds to make a distinction between PCs and PSs. Previous studies based on TRMM Precipitation Rader (PR) have defined a rain cell as adjacent grid boxes showing the precipitation rate $\geq 0.5 \, \mathrm{mm \, h^{-1}}$ (e.g., Jiang et al. 2011; Li et al. 2018), which is the lowest light precipitation that TRMM PR can capture. From TRMM, this lowest light precipitation rate threshold ($\geq 0.5 \, \mathrm{mm \, h^{-1}}$) captures 97% of surface rain amount (Schumacher and Houze 2003), whereas the most frequently detected heavy rain rate over tropical and subtropical ocean is $5 \, \mathrm{mm \, h^{-1}}$ (Berg et al. 2010).

Figure 2 demonstrates how these thresholds associate with tropical storms in IMERG: precipitation rate $\geq 5 \, \mathrm{mm \, h^{-1}}$ (Fig. 2a) captures most of the heavy rain cells near the convection, whereas precipitation rate $\geq 0.5 \, \mathrm{mm \, h^{-1}}$ (Fig. 2b) also

TABLE 1. Spatial correlation coefficients between Tb and PR with different thresholds at 0000 1 Jan 2008.

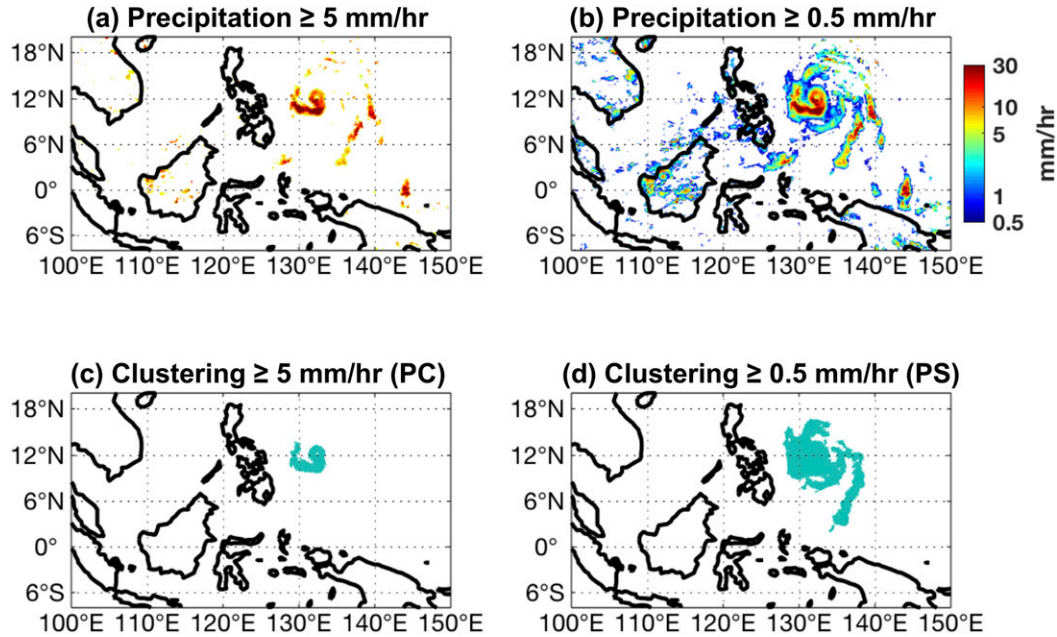|	PR $> 0.01 \, \mathrm{mm \, h^{-1}}$	PR $> 0.5 \, \mathrm{mm \, h^{-1}}$	PR $> 5 \, \mathrm{mm \, h^{-1}}$
Tb < 280 K	−0.27	−0.23	−0.16
Tb < 260 K	−0.27	−0.22	−0.16
Tb < 245 K	−0.26	−0.21	−0.16
Tb < 220 K	−0.26	−0.23	−0.20

FIG. 2. IMERG precipitation rates for (a) precipitation $\geq 5\,\mathrm{mm\,h^{-1}}$, (b) precipitation $\geq 0.5\,\mathrm{mm\,h^{-1}}$, and the largest (c) PC and (d) PS over 90°–150°E and from 8°S to 20°N observed on 0730 UTC 9 May 2008.

includes light precipitation as it captures the majority of rainfall (~70%) in IMERG.

We use these two thresholds to make a distinction between PCs and PSs: a PC is identified as adjacent rainy pixels with the higher threshold ($\geq 5\,\mathrm{mm\,h^{-1}}$) and a PS is identified using the lower threshold ($\geq 0.5\,\mathrm{mm\,h^{-1}}$) when at least one PC is embedded in the PS. In this way PSs are defined to be larger than the PCs and inclusive of the core area. Examples of the largest segmented cluster of PC and its corresponding PS over this region are demonstrated in Figs. 2c and 2d, respectively. The sensitivity to different thresholds will be discussed in section 4.

b. Tracking algorithm

A 3D labeling is applied for PCs based on a 10-connected spatiotemporal neighborhood, composed of an 8-connected spatial neighborhood and a 2-connected temporal neighborhood, similar to Fiolleau and Roca (2013a). In other words, pixels are defined to be connected if their edges or corners touch, and two adjoining pixels (one time step before and

after) are considered to be part of the same object (Fig. 3a). This 3D labeling connects individual PCs into a single family by giving a unique family number. In each time step of a PC, a PS in which the PC is embedded is identified in a way that Fig. 2 illustrates: the PC in Fig. 2c is embedded in the PS in Fig. 2d, and it is possible that more than one PC share the same PS when PCs are closely located. Then, information of location, intensity, and area of the PC, together with the PS in which the PC is embedded, are saved. In this way, we are able to track the evolution of tropical convective storms from PCs and their associated PSs (Fig. 4), including stratiform areas. We also create a flag when a PC experiences merging or splitting. We refer to our convection-tracking dataset to as IMERG-CT and the list of variables available in IMERG-CT is summarized in Table 2.

Vigorous rainfall can be produced by warm-topped systems in moist environment, which cannot be captured by traditional IR-based tracking but is observed in IMERG-CT. Therefore, an advantage of IMERG-CT is its ability to include the
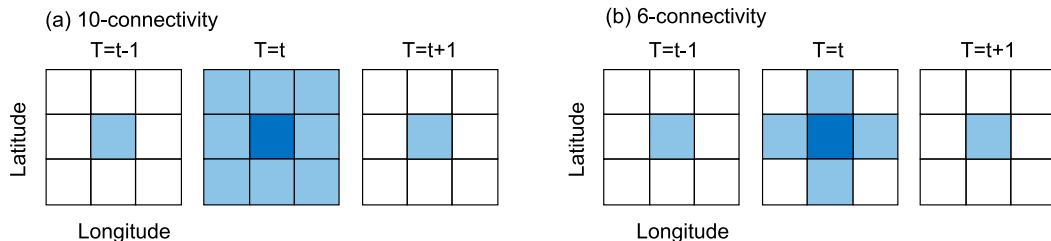

FIG. 3. Illustrations of (a) the 10 connectivity (an 8-connected spatial neighborhood and a 2-connected temporal neighborhood) and (b) the 6 connectivity (a 4-connected spatial neighborhood and a 2-connected temporal neighborhood).
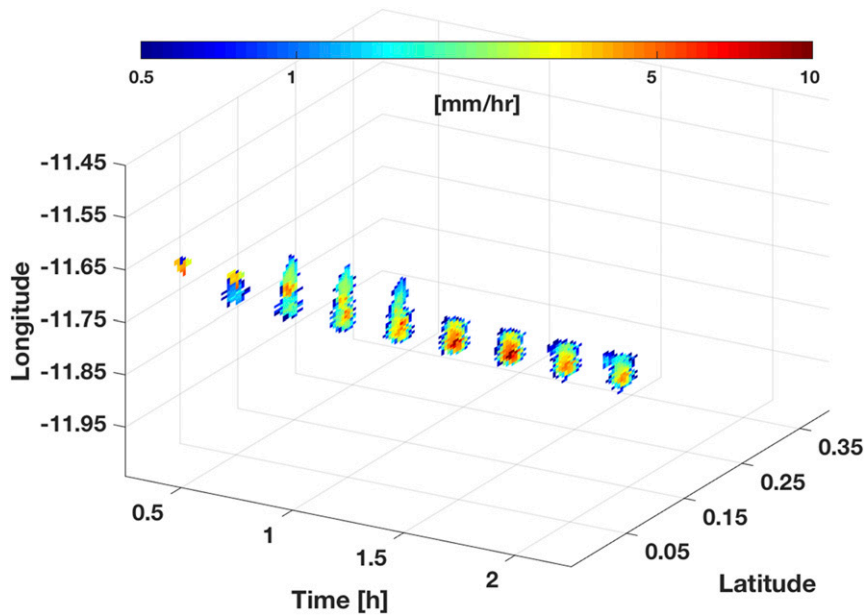
FIG. 4. A demonstration of tracking the evolution of precipitation from a precipitation core and its associated precipitation system.

previously missing information of shallow clouds that grow into convective storms, which provides us more complete life cycle records of convective storms than traditional IR-based tracking does. This means that IMERG-CT may also contain PCs that are only associated with shallow clouds that never have chance to develop deep, because such clouds can produce precipitation rate $> 5\,\mathrm{mm\,h^{-1}}$, which is our definition of PCs. In this study, we would like to exclude such clouds to focus only on life cycles of larger tropical convective storms.

To exclude IMERG-CT families whose PCs are all associated with shallow clouds, we also track life cycles of Tb based on ISCCP-HXG. Recall that the frequency of the ISCCP-HXG data is every 3 h so it is only available once every 6 IMERG time steps. We store the information of Tb for PCs and PSs in IMERG-CT when the observed time between ISCCP-HXG and IMERG matches, and make an additional requirement: an IMERG-CT family must have at least one PC that has minimum Tb $<$ 245 K at some point during the life cycle, the same threshold that is applied to select convective systems in ISCCP-CT. Adding information of Tb into IMERG-CT also helps us in investigating the life cycle correlations between precipitation and Tb and exploring the potential temporal separation between peaks of precipitation and Tb.

4. Evaluation and sensitivity test

a. Comparison with observations from CloudSat

To evaluate the utility of the additional requirement that Tb must reach below the 245 K threshold in at least one instant in the whole lifetime, one month (January 2008) of CloudSat observations (2B-GEOPROF and 2B-GEOPROF-lidar) are collocated with IMERG when the observed time between

CloudSat and IMERG matches. Since CloudSat CPR and IMERG have resolutions of 1.4 and 10 km, respectively, $\sim$10 pixels of CloudSat CPR profiles fall into an IMERG grid box. Therefore, maximum values of cloud-top height (CTH) and cloud thickness based on 2B-GEOPROF-lidar are composited over all PCs, and histograms of these cloud properties are compared between IMERG-CT families with minimum Tb $<$ 245 K and those with minimum Tb $>$ 245 K in Figs. 5a–d. Results clearly show that the requirement of minimum Tb $<$ 245 K can eliminate the majority of low clouds whose CTH and cloud thickness are less than 10 km. Note that CloudSat does not necessarily detect all the deep clouds within a $0.1° \times 0.1°$ grid box due to the nadir sampling

TABLE 2. List of variables available in IMERG-CT.

Family number (unique by year)
Lifetime of this family as number of PS it contains
Max precipitation rates in this family (mm h^{-1})
System total precipitation in this family (kg)
Max PC area in this family (km^2)
Max PS area in this family (km^2)
Min Tb in this family (K)
Min and max lat in this family
Min and max lon in this family
Flag of merging or splitting
Time (year, month, day, and hour)
Min, max, and mean precipitation over each PS (mm h^{-1})
Area total precipitation over each PS (kg)
Min, max, and mean Tb over each PS (K)
Area of each PC and PS (km^2)
Min and max latit over each PS
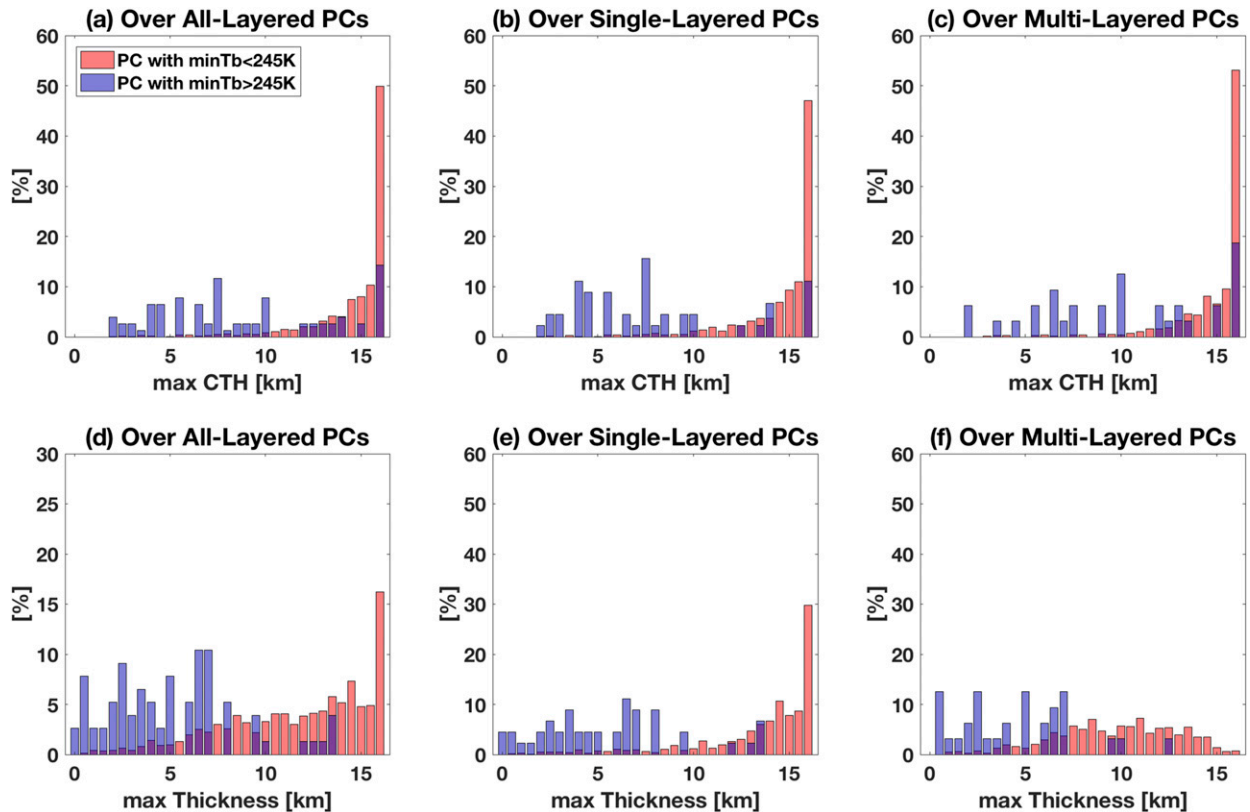Min and max lon over each PS
Fraction of ocean

FIG. 5. Histograms of maximum (top) CTH and (bottom) cloud thickness based on 2B-GEOPROF-lidar that are collocated over (a),(d) all PCs; (b),(e) single-layered PCs; and (c),(f) multilayered PCs, with an assumption that IMERG-CT families must contain at least one PC that has minimum brightness temperature (Tb) < 245 K (red) and one that has minimum Tb > 245 K (blue).

and therefore some of the remaining PCs that *CloudSat* suggests may in fact have deeper cloud in another portion of the grid box. However, another possibility is that some of these remaining cases are multilayered cases that have shallow precipitation beneath a radiometrically cold cirrus that may not be detected by the *CloudSat* radar. To investigate this possibility, maximum values of CTH (Figs. 5b,c) and cloud thickness (Figs. 5e,f) over single- and multilayered PCs are compared. Results confirm that the multilayered cases only explain some remaining cases of shallow clouds, and thus IMERG itself has limitations in excluding shallow clouds. To this end, inclusion of supplementary IR data helps.

CloudSat CPR profiles based on 2B-GEOPROF collocated with PCs and PSs can be conveniently summarized in Fig. 6 through contoured-frequency-by-altitude diagrams (CFAD; Yuter and Houze 1995). Both PCs and PSs have a similar bowlike shape, which is typical of deep convective systems observed by millimeter-wavelength radar from space. The CFAD of PCs shows more occurrence of large radar echo (~10 dBZ) at higher altitudes and more severe attenuation in radar signals at the lower levels than the CFAD of PSs. These features are consistent with the definition of the PCs as having larger rain rates than PSs. Both the PC and PS CFAD show evidence of a radar bright band that is indicative of a melting layer associated with stratiform precipitation. This is a clear

indication that PCs should not be interpreted as only representing convective cores although they may contain convective cores within them.

b. Sensitivity test

1) 10 VERSUS 6 CONNECTIVITIES

As we described above, we apply a 10-connectivity criterion for the 3D labeling. Here, we also test a six-connectivity criterion, composed of a four-connected spatial neighborhood and a two-connected temporal neighborhood, to examine how sensitive the convection tracking is to the selection of connectivities. For the six-connectivity criterion, pixels are defined to be connected if their edges touch, and two adjoining pixels (one-time step before and after) are considered to be a part of the same object (Fig. 3b). Two months (January and February 2008) of IMERG-CT based on the 10 and 6 connectivities are compared in Table 3, which lists the sample sizes of total storm families, fraction of storms that have lifetimes of more than one day or less than 30 min, and that have merging or splitting cases.

Results without (with) applying the assumption of minimum Tb < 245 K show that number of storm families increases by 1.2 times (1.1 times) when using the 6 connectivity rather than the 10 connectivity. This is reasonable because the 10-connectivity
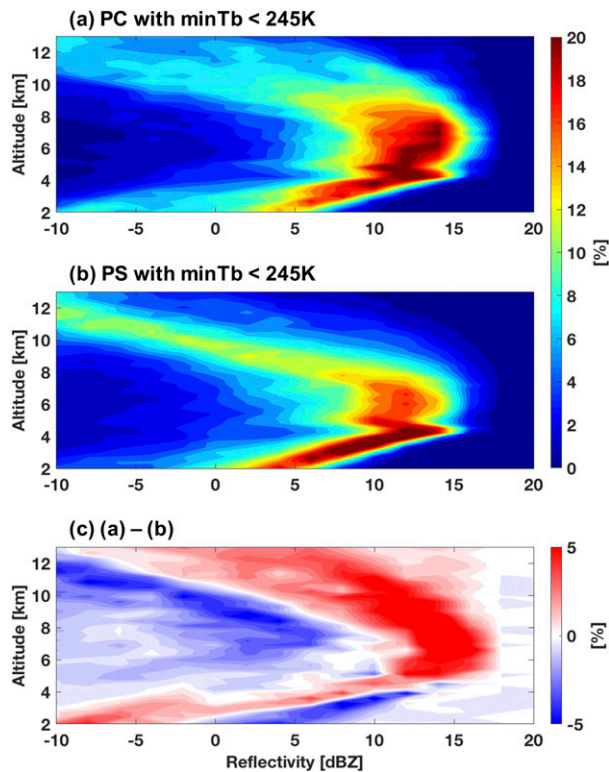
FIG. 6. CFADs based on *CloudSat* CPR reflectivities that are collocated with (a) PC and (b) PS, and (c) the differences between them.

criterion allows more opportunities for pixels to connect with each other, thus has larger families, and thus has fewer labeled families. The fraction of storms whose lifetime exceed more than a day is similar between the two connectivity criteria, but the 6-connectivity criterion favors storms whose lifetime is less than 30 mins by 5.1% (5.7%) relative to the 10-connectivity criterion. We would like to minimize the fraction of storms whose lifetime is less than 30 mins because they only show up in one single image and do not allow us to track their life cycles. We also would like to reduce storms that have merging or splitting cases, but the fractional difference is only 1.2% (2.5%) between the 6- and 10-connectivity criteria. Therefore, we decided to use the 10-connectivity rather than the 6-connectivity criterion in this study.

2) PRECIPITATION RATE THRESHOLDS

The convection tracking is sensitive to the selection of precipitation rate thresholds since it determines the characteristics of PCs and PSs. To test how sensitive the list of variables used in Table 3 is to the selection of precipitation thresholds, the IMERG-CT with different precipitation thresholds is examined. Several previous studies referred rain intensity lower than $1 \, \mathrm{mm \, h^{-1}}$ as light precipitation (e.g., Tian et al. 2018; Tao et al. 2019; Wang et al. 2020) and rain intensity greater than $10 \, \mathrm{mm \, h^{-1}}$ as strong precipitation (e.g., Maranan et al. 2020) or convective precipitation (Cui et al. 2020). Therefore, we apply thresholds from 0.1 to

TABLE 3. IMERG-CT dataset based on 10 and 6 connectivities without or with (in parentheses) applying the assumption of minimum Tb $<$ 245 K.

	10 connectivity	6 connectivity
Total storm family (cases)	642 035 (183 906)	754 312 (201 060)
Lifetime $>$ 1 day (%)	0.06 (0.20)	0.04 (0.17)
Lifetime $=$ 1 step (%)	66.2 (35.5)	71.3 (41.2)
Merging or splitting (%)	5.4 (16.7)	4.2 (14.2)

$0.9 \, \mathrm{mm \, h^{-1}}$ for PSs and those from 1 to $9 \, \mathrm{mm \, h^{-1}}$ for PCs to generate one month (January 2008) of IMERG-CT using 10-connectivities and the assumption of minimum Tb $<$ 245 K. Results are summarized and compared in Table 4. It is clear that the number of storm families decreases as a threshold increases, but the rest of variables are not too sensitive to PS thresholds, especially when PC threshold $\geq 5 \, \mathrm{mm \, h^{-1}}$. We also find out that PC thresholds higher than $5 \, \mathrm{mm \, h^{-1}}$ often fail to capture the entire image of a PC and are likely to break the PC into several subclusters, and PS thresholds lower than $0.5 \, \mathrm{mm \, h^{-1}}$ are not capable of separating individual PSs because multiple clusters are erroneously connected together. In Fig. 7, we use precipitation rate $\geq 20 \, \mathrm{mm \, h^{-1}}$ and precipitation rate $\geq 0.01 \, \mathrm{mm \, h^{-1}}$ as examples to demonstrate the aforementioned issues. As shown in Fig. 7a, precipitation

TABLE 4. IMERG-CT dataset based on different precipitation threshold for PC and PS with 10 connectivities and the assumption of minimum Tb $<$ 245 K.

| PC threshold ($\mathrm{mm \, h^{-1}}$)	PS threshold ($\mathrm{mm \, h^{-1}}$)	Total storm family (cases)	Lifetime $>$ 1 day (%)	Lifetime $=$ 1 step (%)	Merging or splitting (%)
1	0.1	19 793	0.39	40.3	14.9
	0.3	17 667	0.44	40.3	15.9
	0.5	16 133	0.48	39.8	16.7
	0.7	14 679	0.52	39.1	17.8
	0.9	13 295	0.58	37.8	19.0
3	0.1	15 828	0.32	38.2	16.5
	0.3	15 435	0.32	38.2	16.8
	0.5	15 180	0.33	38.0	17.0
	0.7	14 910	0.34	37.8	17.2
	0.9	14 637	0.34	37.5	17.5
5	0.1	12 757	0.15	36.3	16.4
	0.3	12 599	0.15	36.2	16.6
	0.5	12 493	0.15	36.0	16.7
	0.7	12 398	0.15	36.0	16.8
	0.9	12 301	0.15	36.0	16.9
7	0.1	10 209	0.10	34.2	17.0
	0.3	10 146	0.10	34.2	17.1
	0.5	10 101	0.10	34.0	17.2
	0.7	10 061	0.10	34.0	17.2
	0.9	10 016	0.10	34.0	17.3
9	0.1	8353	0.06	33.4	16.6
	0.3	8318	0.06	33.4	16.7
	0.5	8294	0.06	33.3	16.7
	0.7	8271	0.06	33.2	16.7
	0.9	8353	0.06	33.4	16.6
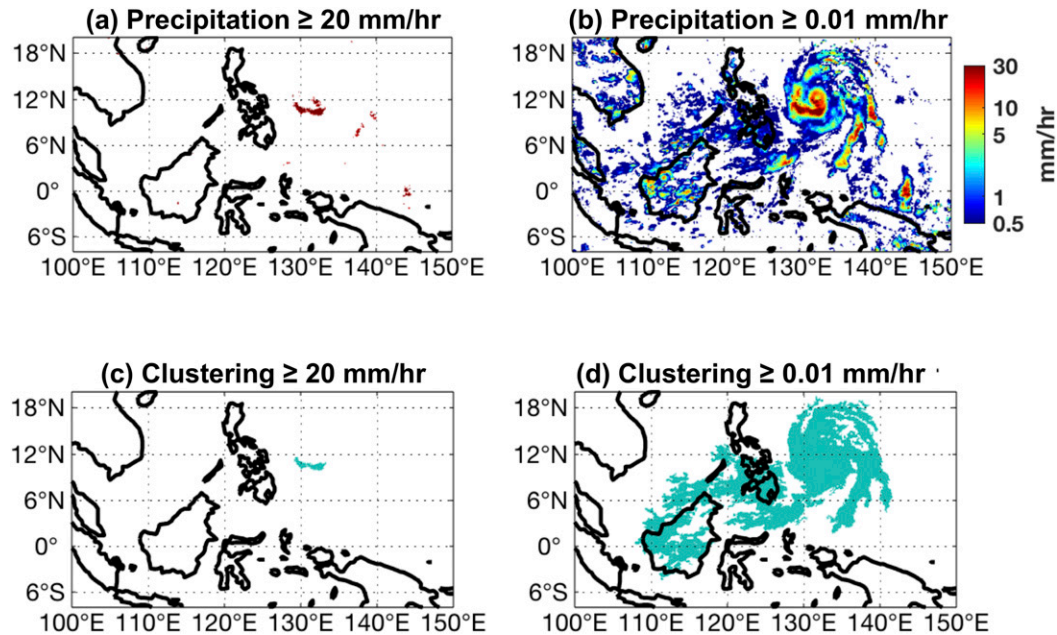
FIG. 7. As in Fig. 2, but using different thresholds: (a),(c) $\geq 20\,\mathrm{mm\,h^{-1}}$ and (b),(d) $\geq 0.01\,\mathrm{mm\,h^{-1}}$.

rate $\geq 20\,\mathrm{mm\,h^{-1}}$ corresponds to very intense rainfall, tracing out only a portion of heavy rain cells in the inner rainbands of a tropical cyclone. As a result, the largest PC in this region becomes too small (Fig. 7c). Precipitation rate as low as $0.01\,\mathrm{mm\,h^{-1}}$ in Fig. 7b, on the other hand, corresponds to very light rain, which ends up connecting multiple PSs together. Therefore, the largest PS in this region becomes too large (Fig. 7d).

3) TROPICAL DOMAIN

Some storms that originally form in the tropics can move to the subtropics as they travel through their lifetime. Since the sample size of storms also depends on location, it is important to know how many tropical convective storms travel outside of tropics. Therefore, we extended our tracking algorithm to 40°S–40°N for one month (January 2008). Results show that only 0.56% of tropical convective storms starting within 20°S–20°N end up outside of 20°S–20°N. Therefore, we decided to use the range of 20°S–20°N for our analysis, realizing that less than 1% of them will leave the domain at some point in their lifetime.

4) CUTOFF SIZE FOR PCs

Although we are using a relatively higher rain rate to define a PC, single pixel overlaps between PCs at two adjacent times easily connect different convective systems that are not related. To reduce uncertainty in artificially connecting precipitation systems and prolonging the lifetime of the precipitation systems, the cutoff size for IMERG-CT is discussed. For example, a system moves 9 km in 30 min if the propagation speed is $5\,\mathrm{m\,s^{-1}}$, or 18 km in 30 min if the propagation speed is $10\,\mathrm{m\,s^{-1}}$. This means that if we assume a system is square, a system smaller than $400\,\mathrm{km^2}$ will likely not overlap itself in

30 min. Therefore, PC sizes are restricted to be greater than $400\,\mathrm{km^2}$.

5. Limitations and uncertainties in IMERG data

Although there are some advantages of using IMERG to study precipitation events, there are inherent limitations and uncertainties in IMERG data, which are worth discussing.

First, unlike IR-based convection tracking where data homogeneity can be achieved (e.g., Fiolleau et al. 2020), IMERG lacks homogeneity in space and time as various sensors (e.g., geostationary IR, microwave sounders and imagers) measure precipitation at different locations and times of the day. Since retrievals and calibrations are not consistent among different sensors, it can cause "flashing" in the precipitation fields as continuous overpasses in a particular location are filled with different sensors (Huffman et al. 2015). Moreover, due to the inhomogeneous nature of the IMERG diurnal sampling, precipitation can fluctuate around the thresholds when the thresholds are exceeded only for certain MW sensors (e.g., Tan et al. 2019). These issues in the performance of the IMERG algorithm can limit the consistency of consecutive snapshots that are needed for IMERG-CT.

Second, IMERG has the selection of a hard-coded threshold for clipping of the intense rain rates. In the IMERG V06, this value is set to $200\,\mathrm{mm\,h^{-1}}$, which is different from the TRMM PR $300\,\mathrm{mm\,h^{-1}}$ threshold (Huffman et al. 2015). This indicates that IMERG clips all the values above $200\,\mathrm{mm\,h^{-1}}$ although the TRMM PR is valid at this range. Also, one of the algorithm modules used in IMERG for the IR-based interpolation of microwave precipitation estimates is the Kalman filter, which tends to smooth out extreme features. These may limit analyzing extreme values in the life cycle and impact the ability to
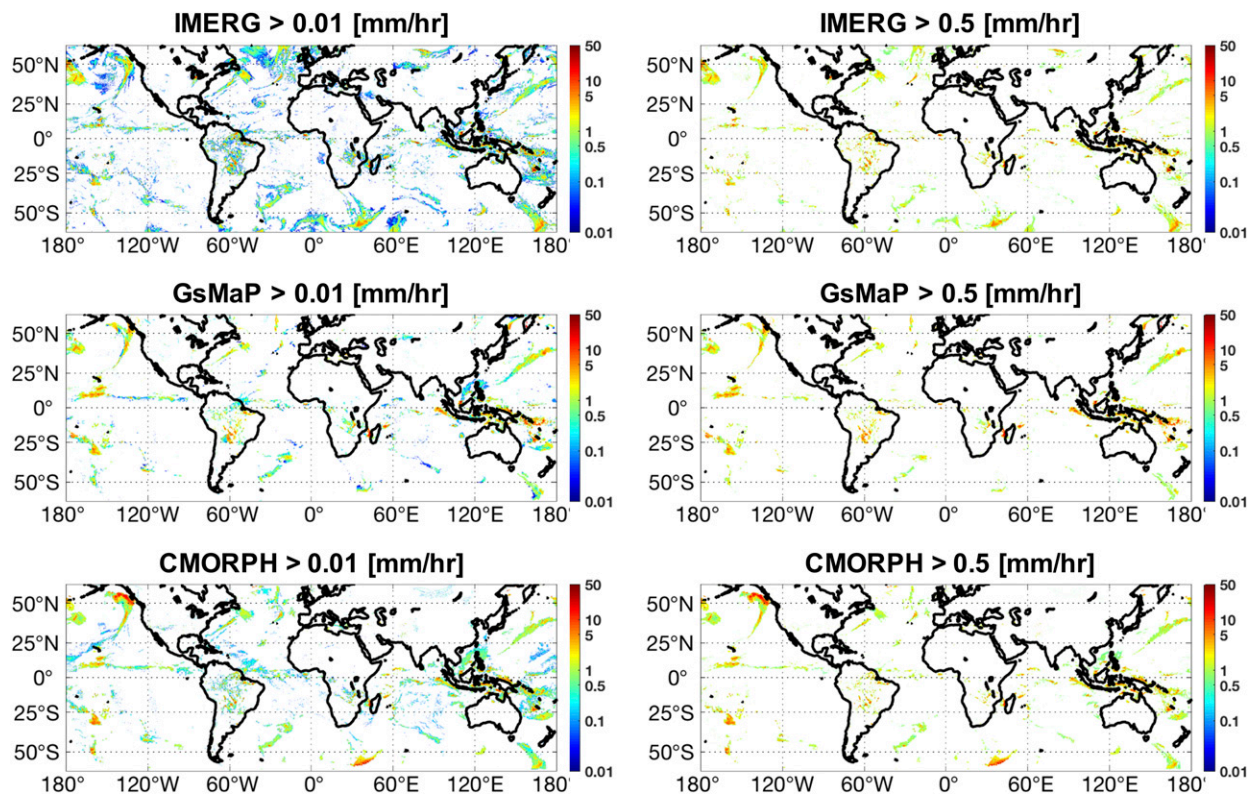
FIG. 8. The global distribution of precipitation rates for (top) IMERG, (middle) GSMaP, and (bottom) CMORPH cut off at (left) 0.01 mm h^{-1} and (right) 0.5 mm h^{-1} thresholds observed on 0000 UTC 1 Jan 2008.

properly describe the mean precipitation properties of the systems. In addition to the Kalman filter, another module used in IMERG is the IR-based PERSIANN (Hsu et al. 1997, 1999, 2007; Sorooshian et al. 2000, 2002; Nguyen et al. 2017, 2018) estimate, which is using the PERSIANN-CSS (Nguyen et al. 2018) version that already includes its own cloud clustering algorithm. The use of such cloud clustering with different thresholds may potentially distort the definition of IMERG-CT. This impact, however, should be minor since sensitivity tests with GSMaP and CMORPH, neither of which adopts the PERSIANN-CSS approach, in lieu of IMERG as demonstrated below do not qualitatively alter the results.

Third, the IMERG product depends critically on MW retrievals by the Goddard profiling algorithm (GPROF) (Kummerow et al. 2015). This means that continental retrievals depend on microwave-scattering signals from solid hydrometeors. Thus, IMERG results are less reliable for shallow precipitation without ice processes over land. Therefore, IMERG-CT can contain some uncertainty for shallow clouds over land (Zhou et al. 2019). It is noted that satellite estimates are calibrated to gauge-network data over land for IMERG so the known deficiencies in continental warm-rain retrieval from space are partially mitigated.

A recent study comparing IMERG V06 and radar-based product in MCSs finds that IMERG consistently overestimate rainfall amounts from light and moderate precipitation (<10 mm h^{-1}), particularly precipitation between 1 and

10 mm h^{-1} over the continental United States (Cui et al. 2020). Another recent study also pointed out that IMERG tends to overestimate frequently occurring weak convective events, while it tends to underestimate rarely occurring strong meso-scale convective systems, resulting in an error compensation (Maranan et al. 2020). The accuracy of IMERG retrievals, namely at lower rain rates has not been well established.

The abovementioned limitations and uncertainties can impact our results based on IMERG-CT. A useful approach to quantify such uncertainties is to repeat the current analysis with other precipitation datasets in lieu of IMERG to see how the results change. In this way, the potential issues specific to IMERG would be able to separate from general limitations common to different products. To this end, we compare IMERG with GSMaP and CMORPH. IMERG overall captures wider areas of precipitation than GSMaP/CMORPH and there are some systematic product-dependent biases in precipitation rates. However, the distributions of precipitation events with thresholds of precipitation rate >0.5 mm h^{-1} (our definition of PS) are comparable between IMERG and GSMaP/CMORPH (Fig. 8). We also generate one-day statistics of CT datasets based on CMORPH and GSMaP and compare the results with IMERG-CT on the same day (Table S1 and Figs. S1 and S2 in the online supplemental material). Results clearly show that they all share similar aspects of the cluster properties, except for the maximum precipitation rate. IMERG tends to have higher maximum precipitation
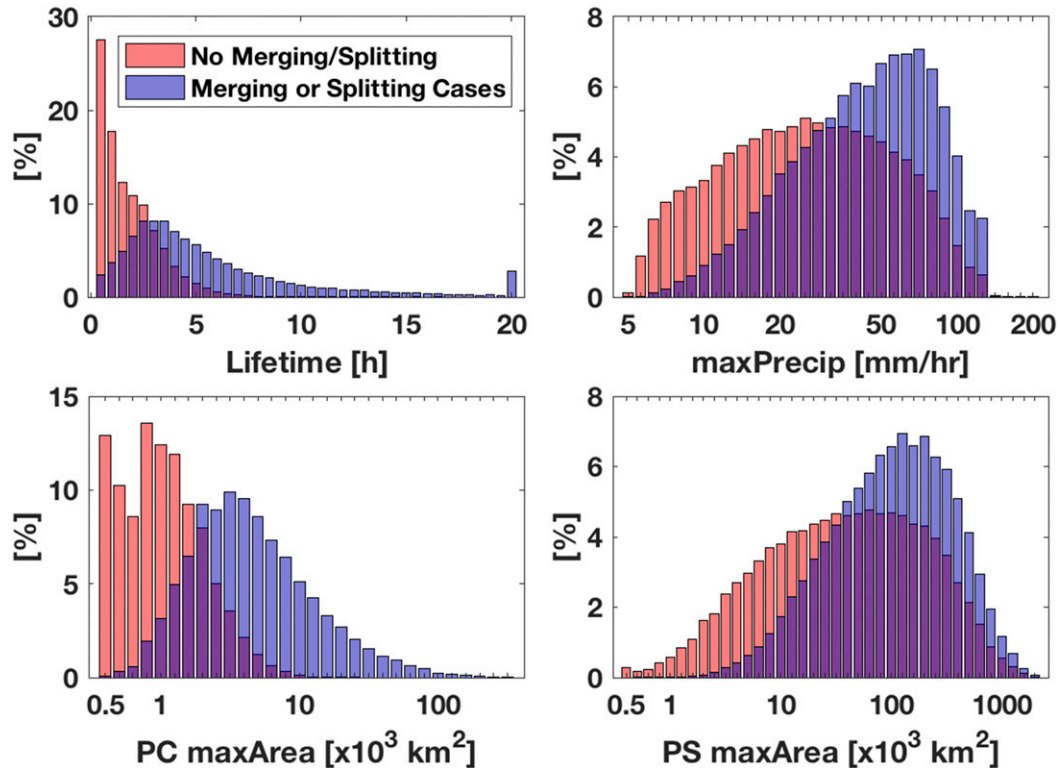
FIG. 9. Histograms of lifetime duration of each storm family, together with maximum precipitation, maximum area of PC, and maximum area of associated PS among each storm family that has no merging or splitting cases (blue) and that has some merging or splitting cases (red). Histograms are normalized so that the red and blue bar heights add to 100% separately.

rate than GSMaP/CMORPH. This is consistent with Masunaga et al. (2019), which shows that in the 99th percentile extremes, IMERG exceeds GSMaP and CMORPH at all latitudes. Moreover, the flashing effect is not noticeable when precipitation $> 5 \, \mathrm{mm \, h^{-1}}$. The comparison suggests that clipping of intense rainfall and using of Kalman filter did not entirely remove extreme features in IMERG, and the lack of homogeneity and associated flashing effect in IMERG data do not bring large uncertainties in IMERG-CT when we use PC $> 5 \, \mathrm{mm \, h^{-1}}$.

Although there are some inherent limitations and uncertainties in IMERG data, they seem not to bring serious errors in IMERG-CT. Also, as IMERG V06 made great improvement on studying the diurnal cycle compering to the previous version of V05 (Tan et al. 2019), IMERG continues to be improved with known issues solved by the developers, and these improvements flow down to our IMERG-CT. This is a flexible framework of the method and keeps evolving as the IMERG gets improved in the future.

a. Surveys over the tropics

Based on the evaluations and sensitivity tests, we use precipitation rate $\geq 5 \, \mathrm{mm \, h^{-1}}$ and precipitation rate $\geq 0.5 \, \mathrm{mm \, h^{-1}}$ thresholds to define PCs and PSs, respectively. We finalize the procedure by using 10-connectivity 3D labeling and applying the condition of at least one occurrence of minimum Tb $<$ 245 K and generate two years (January–December 2007 and 2008) of IMERG-CT over 20°S–20°N to track the evolution of

tropical convective storms. Here we show some of the statistical properties of the tracked convective systems. Because the primary purpose of this paper is to describe the tracking algorithm and dataset, this is not a comprehensive exploration. Rather we seek to highlight some interesting features of the dataset.

b. Statistics of convective storm properties

Histograms of lifetime duration and maximum precipitation rate for IMERG-CT, as well as maximum area of PCs and their associated PSs are investigated in Fig. 9 through a comparison between IMERG-CT families without (red) and with (blue) merging/splitting storms. Note that about 17% of IMERG-CT families have merging/splitting storms (Table 3) and histograms are normalized so that each red and blue bar heights add to 100% separately. IMERG-CT families with merging/splitting storms have longer lifetime durations than those without, and storms with longer lifetimes tend to be bigger and to produce stronger precipitation rate than those with shorter lifetimes. Therefore, it is not surprising to see IMERG-CT families with merging/splitting storms tend to have higher maximum precipitation rates and larger maximum area of PCs and PSs that those without merging/splitting storms.

c. Spatial distributions

To understand how the tropical convective storms in IMERG-CT are distributed over the tropics (20°S–20°N), we
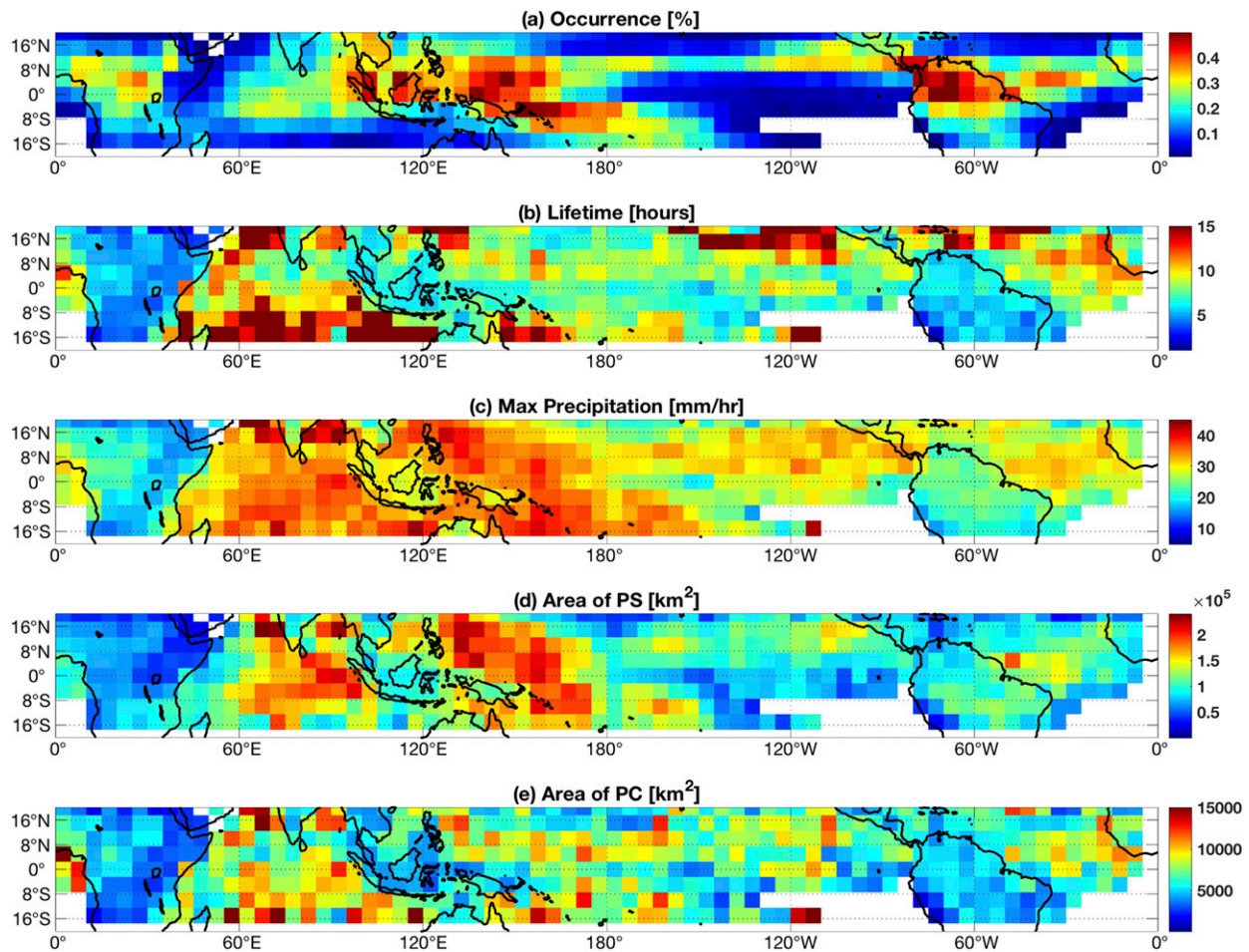
FIG. 10. Tropical maps of (a) occurrence frequency, (b) lifetime, (c) maximum precipitation, (d) area of precipitating systems, and (e) area of precipitating cores of precipitating storms in 5° × 5° boxes over 20°S–20°N. Those grid boxes with occurrence frequency of precipitating storms less than 0.01% are left blank.

explore the spatial patterns of occurrence frequency, together with annual mean value of lifetime duration, intensity of precipitation, and size of IMERG-CT families (Fig. 10). Similar to Liu et al. (2008), Fig. 10a shows that tropical convective storms are most prevalent over the following five regions: tropical Africa, Amazon, tropical warm pool, eastern Pacific intertropical convergence zone (ITCZ), and Atlantic ITCZ, where deep convective clouds appear prominently (e.g., Liu et al. 2007; Takahashi and Luo 2014). Figure 10b shows that continental storms generally have shorter lifetime durations than oceanic storms, which is consistent with previous studies (e.g., Futyan and Del Genio 2007), and long-lived storms are concentrated around 20°N over the Arabian Sea, the Bay of Bengal, the northeast Pacific Ocean, and the northeast Atlantic Ocean, or around 20°S over the Indian Ocean. These long-lived storms around 20°N are observed during northern summer (June, July, and August), and those around 20°S are observed during southern summer (December, January, and February). Extratropical cyclones are generally more frequent during the winter season near 40°N/S latitudes. Therefore, these long-lived storms in local summer can be due to the invasion of

extratropical cyclones into the lower latitudes during the summer season. Maximum precipitation rate (Fig. 10c) is the highest over the warm pool, and remains high over Africa, Amazon, eastern Pacific ITCZ, and Atlantic ITCZ, similar to the regions in Fig. 10a where deep convective clouds are prevalent. The largest areal coverages by PSs (Fig. 10d) are also observed over the warm pool, ITCZ, and Amazon. For the area of PCs (Fig. 10e), a clear land–ocean contrast is found: PCs are likely to be smaller over land than ocean. The land–ocean contrast is also present in the PS area, although not as striking as in the PC area. It is evident when compared between the Maritime Continent and the surrounding oceans. As found in many previous studies (e.g., Houze and Cheng 1977; Chen et al. 1996; Machado et al. 1998), larger storms tend to be longer lived, which is evident from the land–ocean contrast in this study.

d. Life cycles

Figure 11 shows the life cycle evolution of the following IMERG-CT variables, sorted by lifetime duration categories: PC area, PS area, fraction of PC to PS area, maximum
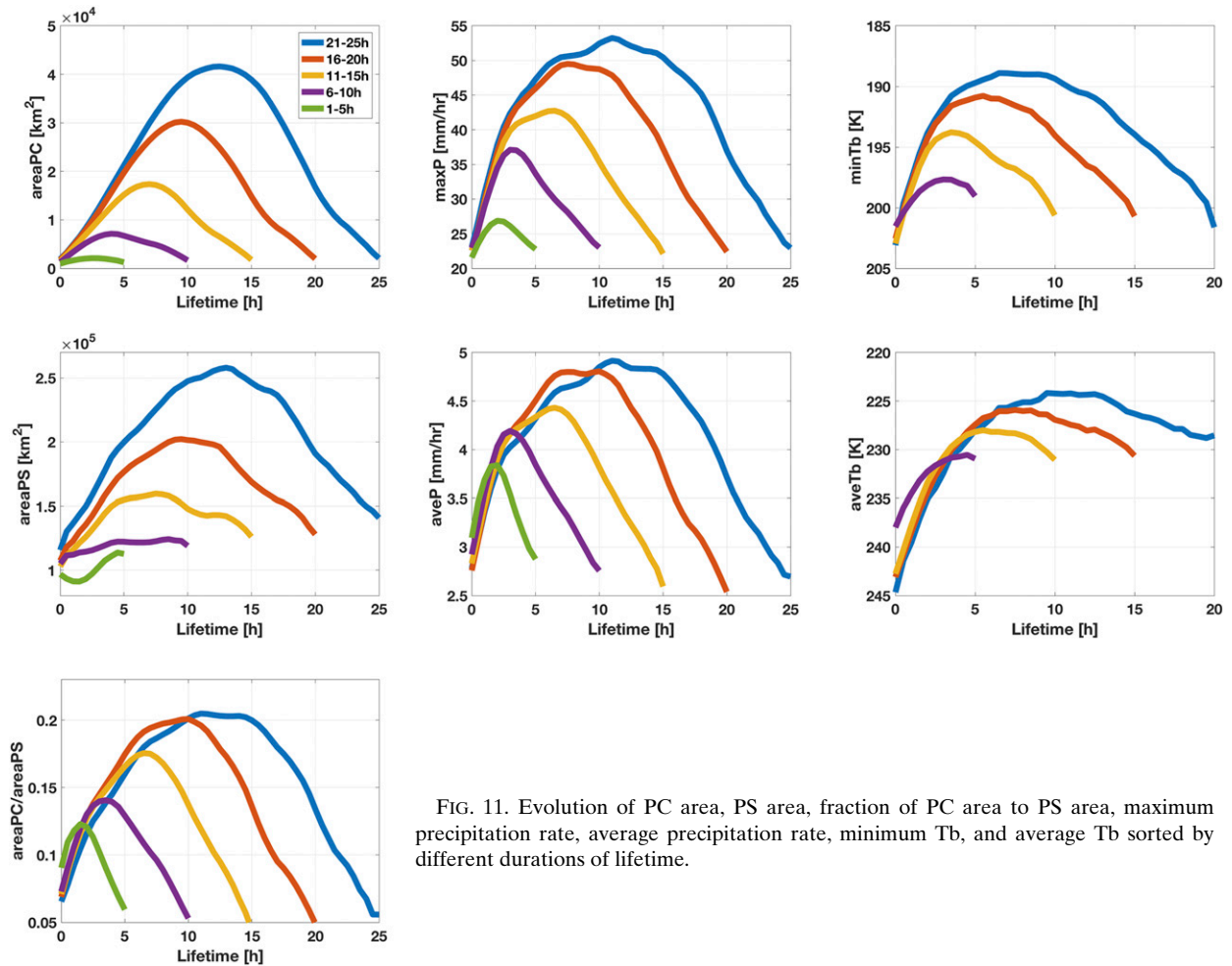
FIG. 11. Evolution of PC area, PS area, fraction of PC area to PS area, maximum precipitation rate, average precipitation rate, minimum Tb, and average Tb sorted by different durations of lifetime.

precipitation rate, average precipitation rate, minimum Tb, and average Tb. We have 140 418 samples for 1–5 h duration, 20 467 samples for 6–10 h duration, 5265 samples for 11–15 h duration, 1873 samples for 16–20 h duration, and 827 samples for 21–25 h duration. The evolutions of PC and PS areas have about the same shape over all lifetimes, and they increase to peak size at about midlife. The storm families with longer lifetime show larger PC and PS areas, colder Tb, and higher precipitation rate at their peaks. These results are consistent with Machado et al. (1998) and Inoue et al. (2009), although these previous works focused on clouds while our current study focuses on precipitation. The initial growth rates of IMERG-CT variables are also explored as in Machado et al. (1998), which suggested that they can be good indicators for the life-time duration of storms. We examine the initial growth rates (difference between first two time steps) and find that the initial growth rates of PC area, PS area, and maximum precipitation rate tend to be higher for long-lasting storm families, which is consistent with other studies (e.g., Machado and Laurent 2004). It is also found that Tb reaches its minimum earlier than the PS area reaches its maximum, which is consistent with other studies (McAnelly and Cotton 1989; Arnaud et al.

1992; Futyan and Del Genio 2007; Takahashi and Luo 2014). For the precipitation rate (both maximum and averaged), the peak comes usually before the PC or PS area reach its peak. It is interesting to point out that the evolution of fraction of PC to PS area follows that of precipitation rate, reaching its maximum at about the same time precipitation rate reaches maximum. Therefore, the storm families with longer lifetime have a higher precipitation rates and a larger fraction of PC to PS area.

e. Dependence of system total precipitation of PS characteristics

Figure 11 demonstrates how IMERG-CT can be used to study precipitation evolution from the Lagrangian perspective. Based on IMERG-CT, we can also estimate system total precipitation by integrating area total precipitation of a PS over its lifetime. This means that we can now study total rainfall based on Lagrangian accumulations rather than Eulerian accumulations, which is a very important step in diagnosing cloud-precipitation process following the evolution of air masses. Here, we investigate how the amount of system total precipitation depends on lifetime and intensity of storm families. Figures 12a and 12b show system total precipitation
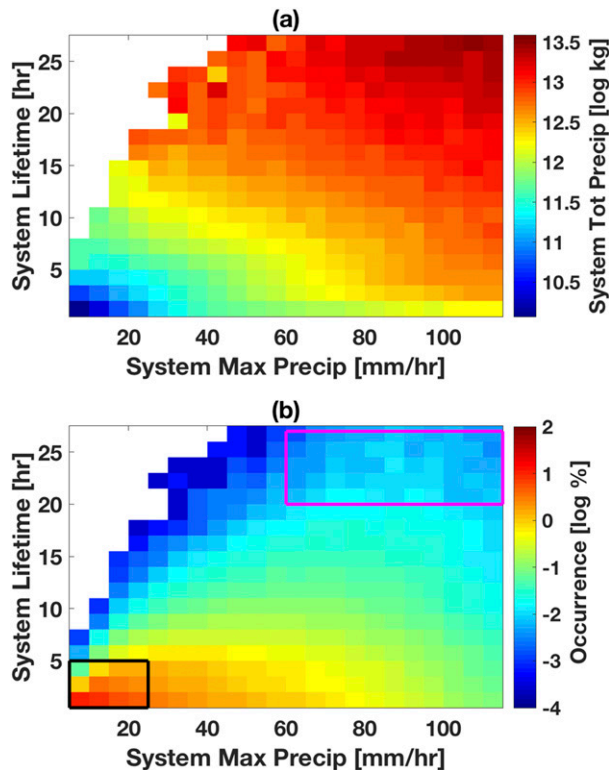
FIG. 12. (a) System-total precipitation and (b) occurrence frequencies as functions of system maximum precipitation (*x* axis) and system lifetime (*y* axis). Black- and magenta-outlined boxes in (b) are examples of weaker shorter-lived PS families and stronger longer-lived PS families, respectively.

and occurrence frequency of storm families as functions of system lifetime and highest precipitation rate among a storm family (system maximum precipitation rate), respectively. Results show that system total precipitation is equally sensitive to lifetime and precipitation rates as weaker shorter-lived PS families produce less system total precipitation than stronger longer-lived PS families, which is expected. However, it is worth pointing out that those weaker shorter-lived PS families are more frequently occurring relative to those stronger longer-lived PS families. For example, 51.9% of PS families fall into the black box in Fig. 12b, yet they only contribute 0.1% of total precipitation over the tropics. On the other hand, although only 0.5% of PS families fall into the pink box in Fig. 12b, they contribute 48.6% of total precipitation over the tropics. Based on Fig. 10, it is known that stronger longer-lived PS families are likely to be larger systems. These results highlight that large portion of tropical rainfall are due to rarely occurring PS families that are probably mesoscale-organized type of convective systems (e.g., Mohr et al. 1999; Rossow et al. 2013).

f. Linkage between rainfall and cloud-top temperature

As discussed before (section 2d), correlations between instantaneous precipitation rate and Tb images are low because higher clouds do not always generate more rainfall than lower clouds. However, some consistent patterns start to show up

when comparisons are made between composite life cycles of precipitation and Tb: storm families with longer lifetime tend to have higher precipitation rate and colder Tb than the storm families with shorter lifetime (Fig. 11). To further clarify the linkages between precipitation and Tb through investigating the time lag between precipitation and Tb, we investigate the coevolution between precipitation and Tb for each IMERG-CT family by anchoring Tb on precipitation through a composite method similar to the one introduced by Masunaga (2012, 2013).

The composite time series is constructed for investigating various properties of convective systems in terms of the evolution before and after peak precipitation. First, the time lag between the evolution of maximum precipitation rate (the highest precipitation rate over an area of PS) and that of minimum Tb (the lowest Tb over an area of PS) is investigated. Since each family has its own timing to reach its own peak value of maximum precipitation rate that is highly variable from 5 to 197 mm h^{-1}, we estimate fractional maximum precipitation rate relative to the peak value of maximum precipitation rate during the life cycle of each family and set composite time to be 0 when the maximum precipitation reaches the peak value during its lifetime. For minimum Tb, we examine the anomaly against its coldest value within the family since the anomaly better illustrates the magnitude of variability than raw infrared Tb. We compare the evolution of fractional maximum precipitation rate and the anomalous minimum Tb as a function of composite hours built around the maximum precipitation rate. In this way, fractional maximum precipitation rate is by construction 100% when the composite time is 0, and the temporal variation of minimum Tb relative to the hour of peak precipitation can be clearly visualized. We do not include the families that have multiple peaks of maximum precipitation rate or minimum Tb. In the same manner, the composite time series of different parameters are also investigated, and results are summarized in Fig. 13.

Figures 13a and 13c show the temporal sequence of fractional maximum precipitation rate and anomalous minimum Tb, and that of fractional maximum precipitation rate and average Tb, respectively. Minimum Tb reaches its peak at composite time equals to 0, which means that temporal separations between maximum precipitation and minimum Tb is within 3 h or the temporal resolution adopted in this study. An interesting point of this composite analysis lies in the difference between the behaviors of minimum Tb and average Tb. Unlike minimum Tb that has rapid decreases after the convective rain peaks, average Tb mostly stay largely the same for 5 h after the peaks. Considering the definitions of these Tb measures, minimum Tb most likely represents the cloud top of convective core, while average Tb characterizes the rest of the storms, mainly stratiform rain and cirrus anvils (Machado and Rossow 1993). The fact that minimum Tb drops off quickly while average Tb stays largely the same for an extended period of time suggests that convective precipitation has a much shorter duration than stratiform precipitation. Figure 13 reveals the signature of stratiform anvils persisting well after the storm has produced the maximum rainfall, which may have significant implications for the time evolution of the latent and radiative
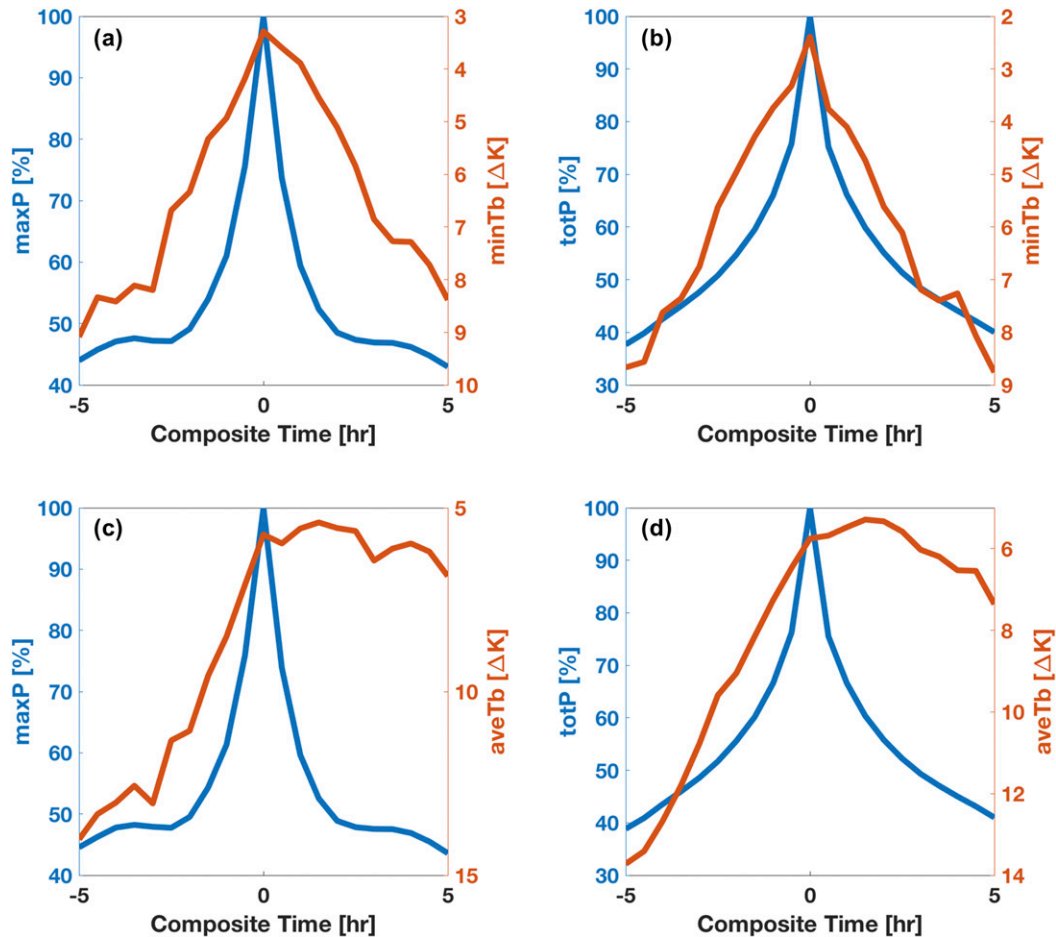
FIG. 13. The composite time series of (a) maximum precipitation rate and minimum Tb, (b) area total precipitation and minimum Tb, (c) maximum precipitation rate and average Tb, and (d) area total precipitation and average Tb.

heating profiles of the storms. Our study highlights the importance of joint analysis of cloud and precipitation data in time sequence, which helps elucidate the underlying dynamic processes producing tropical rainfall and its resultant effects on the atmospheric thermodynamics.

Replacing maximum precipitation rate with total precipitation (PS area total at one time), we further investigate a time lag between the evolution of total precipitation and minimum Tb and that between total precipitation and average Tb, which are shown in Figs. 13b and 13d, respectively. Results again indicate that time delays between total precipitation and minimum Tb is within 3 h, and average Tb mostly stay the same for 5 h after convective rain peaks although minimum Tb have rapid decreases after the peak of total precipitation. Therefore, the signature of stratiform anvils is robust and can be captured by IMERG-CT dataset.

6. Summary

This study is the first attempt to detect and track the evolution of tropical convective storms using the high spatiotemporal imagery of precipitation from IMERG. It differs from

prior efforts to track tropical convective storms in using precipitation as the tracked variable instead of the Tb. We demonstrate that precipitation can be a natural variable upon which to base a convective storm tracking algorithm and Tb does have the natural advantage as a filter of shallow precipitation. This capability is maintained in the algorithm described here through the imposition of a once-per-storm Tb threshold. An additional motivation for using the IMERG data is the purely practical consideration that among existing gridded datasets, IMERG offers 30-min temporal resolution whereas ISCPP-HXG offers only 3-hourly resolution.

The convection-tracking algorithm used in this study goes as follows:

1) Identify PCs (precipitation $\geq 5\,\mathrm{mm\,h^{-1}}$) and PSs (precipitation $\geq 0.5\,\mathrm{mm\,h^{-1}}$) between 20°S and 20°N latitude.
2) A 3D labeling (latitude/longitude/time) is applied for PCs based on a 10-connected spatiotemporal neighborhood (Fiolleau and Roca 2013a) in order to connect individual PCs into a single family by giving a unique family number.
3) Each single family must have at least one time step that has minimum Tb < 245 K in order to exclude shallow clouds

that never grow into deep convective storms. Information on minimum Tb is calculated from the collocated ISCCP-HXG available every 3 h.

4) PC sizes are restricted to be greater than $400 \, km^2$.

Using this algorithm, we generate one year of a convection-tracking dataset, named IMERG-CT. IMERG-CT has been evaluated against *CloudSat* and previous studies in this paper, which confirms that this simple algorithm of convection tracking based on IMERG performs comparably to existing tracking algorithms. However, an advantage of IMERG-CT is its ability to include the previously missing information of shallow clouds that grow into convective storms, which provides us more complete life cycle records of convective storms than traditional IR-based tracking does. We emphasize that up to now precipitation datasets have been Eulerian accumulations whereas with IMERG-CT, it is now possible to study both the time evolution of ''instantaneous'' precipitation rate but also lifetime-accumulated precipitation amount over each convective storm, which is a very important step in diagnosing cloud-precipitation processes in tropical convective storms. Some preliminary characteristics of IMERG-CT shown here are as follows:

1) Continental storms have shorter lifetime durations than oceanic storms, which is consistent with previous studies (e.g., Futyan and Del Genio 2007).

2) Maximum precipitation is the highest over the warm pool, and relatively high over Africa, Amazon, eastern Pacific ITCZ, and Atlantic ITCZ, where deep convective clouds appear prominently, which is consistent with previous studies (e.g., Liu et al. 2008).

3) The storm families with longer lifetimes show larger PC and PS areas, colder Tb, and higher precipitation at their peaks, which is consistent with previous studies (e.g., Machado et al. 1998; Inoue et al. 2009).

4) The initial growth rates of PC area, PS area, and maximum precipitation are higher for long-lasting storm families, which is consistent with previous studies (e.g., Machado and Laurent 2004).

5) The largest PC begins to decrease in size earlier than the PS does, which is similar to Machado et al. (1998), and minimum Tb reaches its minimum earlier than the PS area reaches its maximum, which is consistent with previous studies (McAnelly and Cotton 1989; Arnaud et al. 1992; Futyan and Del Genio 2007; Takahashi and Luo 2014).

6) Nearly half the total precipitation amount over the tropics is produced by rarely occurring (less than 1%) strong long-lived PS families, which are probably associated with mesoscale-organized type of convective systems (e.g., Mohr et al. 1999; Rossow et al. 2013).

7) Composite analysis reveals a link between precipitation and Tb: the signature of stratiform anvils hanging around after the storm has produced the maximum rainfall as average Tb mostly stay almost constant for 5 h after the peak of precipitation.

This study demonstrates the utility of IMERG-CT to analyze the evolution of tropical convective storms and investigate the linkage between precipitation and Tb. Since IMERG has high spatiotemporal resolutions, IMERG-CT might give direct insight on moist convective processes from Lagrangian perspectives. A similar analysis should be applied to extratropical frontal convection. Our future plan is to extend IMERG-CT to multiple years and to study convective evolution and its relation to the thermodynamic environment.

Data availability statement. The data of IMERG can be retrieved from the STORM Processing Center (https://storm.pps.eosdis.nasa.gov/storm/), *CloudSat* observations can be retrieved from the CloudSat Data Processing Center (www.cloudsat.cira.colostate.edu), ISCCP-CT and ISCCP-HXG can be retrieved from https://isccp.giss.nasa.gov/outgoing/PICKUP/CT/ and https://www.ncdc.noaa.gov/isccp/isccp-data-access, respectively.

REFERENCES

Anjum, M. N., and Coauthors, 2018: Performance evaluation of latest integrated multi-satellite retrievals for Global Precipitation Measurement (IMERG) over the northern highlands of Pakistan. *Atmos. Res.*, **205**, 134–146, https://doi.org/10.1016/j.atmosres.2018.02.010.

Arnaud, Y., M. Desbois, and J. Maizi, 1992: Automatic tracking and characterization of African convective systems on Meteosat pictures. *J. Appl. Meteor.*, **31**, 443–453, https://doi.org/10.1175/1520-0450(1992)031<0443:ATACOA>2.0.CO;2.

Ashouri, H., K.-L. Hsu, S. Sorooshian, D. K. Braithwaite, K. R. Knapp, L. D. Cecil, B. R. Nelson, and O. P. Prat, 2015: PERSIANN-CDR: Daily precipitation climate data record from multisatellite observations for hydrological and climate studies. *Bull. Amer. Meteor. Soc.*, **96**, 69–83, https://doi.org/10.1175/BAMS-D-13-00068.1.

Berg, W., T. L'Ecuyer, and J. M. Haynes, 2010: The distribution of rainfall over oceans from spaceborne radars. *J. Appl. Meteor. Climatol.*, **49**, 535–543, https://doi.org/10.1175/2009JAMC2330.1.

Beucher, F., J. P. Lafore, F. Karbou, and R. Roca, 2014: High-resolution prediction of a major convective period over West Africa. *Quart. J. Roy. Meteor. Soc.*, **140**, 1409–1425, https://doi.org/10.1002/qj.2225.

Brocca, L., and Coauthors, 2014: Soil as a natural rain gauge: Estimating global rainfall from satellite soil moisture data. *J. Geophys. Res. Atmos.*, **119**, 5128–5141, https://doi.org/10.1002/2014JD021489.

Chen, S. S., R. A. Houze Jr., and B. E. Mapes, 1996: Multiscale variability of deep convection in relation to large-scale circulation in TOGA COARE. *J. Atmos. Sci.*, **53**, 1380–1409, https://doi.org/10.1175/1520-0469(1996)053<1380:MVODCI>2.0.CO;2.

Coppin, D., G. Bellon, A. Pletzer, and C. Scott, 2020: Detecting and tracking coastal precipitation in the tropics: Methods and insights into multiscale variability of tropical precipitation. *J. Climate*, **33**, 6689–6705, https://doi.org/10.1175/JCLI-D-19-0321.1.

Cui, W., X. Dong, B. Xi, Z. Feng, and J. Fan, 2020: Can the GPM IMERG Final product accurately represent MCSs' precipitation characteristics over the central and eastern United States? *J. Hydrometeor.*, **21**, 39–57, https://doi.org/10.1175/JHM-D-19-0123.1.

Dias, J., N. Sakaeda, G. N. Kiladis, and K. Kikuchi, 2017: Influences of the MJO on the space-time organization of tropical convection. *J. Geophys. Res. Atmos.*, **122**, 8012–8032, https://doi.org/10.1002/2017JD026526.

Feng, Z., X. Dong, B. Xi, S. A. McFarlane, A. Kennedy, B. Lin, and P. Minnis, 2012: Life cycle of midlatitude deep convective systems in a Lagrangian framework. *J. Geophys. Res.*, **117**, D23201, https://doi.org/10.1029/2012JD018362.

Fiolleau, T., and R. Roca, 2013a: An algorithm for the detection and tracking of tropical mesoscale convective systems using infrared images from geostationary satellite. *IEEE Trans. Geosci. Remote Sens.*, **51**, 4302–4315, https://doi.org/10.1109/TGRS.2012.2227762.

——, and ——, 2013b: Composite life cycle of tropical mesoscale convective systems from geostationary and low Earth orbit satellite observations: Method and sampling considerations. *Quart. J. Roy. Meteor. Soc.*, **139**, 941–953, https://doi.org/10.1002/qj.2174.

——, ——, S. Cloché, D. Bouniol, and P. Raberanto, 2020: Homogenization of geostationary infrared imager channels for cold cloud studies using Megha-Tropiques/ScaRaB. *IEEE Trans. Geosci. Remote Sens.*, **58**, 6609–6622, https://doi.org/10.1109/TGRS.2020.2978171.

Funk, C. C., and Coauthors, 2014: A quasi-global precipitation time series for drought monitoring. U.S. Geological Survey Data Series 832, 4 pp., https://doi.org/10.3133/ds832.

Futyan, J. M., and A. D. Del Genio, 2007: Deep convective system evolution over Africa and the tropical Atlantic. *J. Climate*, **20**, 5041–5060, https://doi.org/10.1175/JCLI4297.1.

Gosset, M., M. Alcoba, R. Roca, S. Cloché, and G. Urbani, 2018: Evaluation of TAPEER daily estimates and other GPM-era products against dense gauge networks in West Africa, analysing ground reference uncertainty. *Quart. J. Roy. Meteor. Soc.*, **144**, 255–269, https://doi.org/10.1002/qj.3335.

Griffith, C. G., W. L. Woodley, P. G. Grube, D. W. Martin, J. Stout, and D. N. Sikdar, 1978: Rain estimation from geosynchronous satellite imagery—Visible and infrared studies. *Mon. Wea. Rev.*, **106**, 1153–1171, https://doi.org/10.1175/1520-0493(1978)106<1153:REFGSI>2.0.CO;2.

Hamada, A., Y. N. Takayabu, C. Liu, and E. J. Zipser, 2015: Weak linkage between the heaviest rainfall and tallest storms. *Nat. Commun.*, **6**, 6213, https://doi.org/10.1038/ncomms7213.

Hong, Y., K. L. Hsu, S. Sorooshian, and X. Gao, 2004: Precipitation estimation from remotely sensed imagery using an artificial neural network cloud classification system. *J. Appl. Meteor.*, **43**, 1834–1853, https://doi.org/10.1175/JAM2173.1.

Hou, A. Y., and Coauthors, 2014: The Global Precipitation Measurement Mission. *Bull. Amer. Meteor. Soc.*, **95**, 701–722, https://doi.org/10.1175/BAMS-D-13-00164.1.

Houze, R. A., Jr., and C. P. Cheng, 1977: Radar characteristics of tropical convection observed during GATE: Mean properties and trends over the summer season. *Mon. Wea. Rev.*, **105**, 964–980, https://doi.org/10.1175/1520-0493(1977)105<0964:RCOTCO>2.0.CO;2.

Hsu, K. L., X. Gao, S. Sorooshian, and H. V. Gupta, 1997: Precipitation estimation from remotely sensed information using artificial neural networks. *J. Appl. Meteor.*, **36**, 1176–1190, https://doi.org/10.1175/1520-0450(1997)036<1176:PEFRSI>2.0.CO;2.

——, H. V. Gupta, X. Gao, and S. Sorooshian, 1999: Estimation of physical variables from multichannel remotely sensed imagery using a neural network: Application to rainfall estimation. *Water Resour. Res.*, **35**, 1605–1618, https://doi.org/10.1029/1999WR900032.

——, Y. Hong, and S. Sorooshian, 2007: Rainfall estimation using a cloud patch classification map. *Measuring Precipitation from Space*, Springer, 329–342.

Huffman, G. J., and Coauthors, 2007: The TRMM multisatellite precipitation analysis (TMPA): Quasi-global, multiyear, combined-sensor precipitation estimates at fine scales. *J. Hydrometeor.*, **8**, 38–55, https://doi.org/10.1175/JHM560.1.

——, D. T. Bolvin, and E. J. Nelkin, 2015: Integrated Multi-satellitE Retrievals for GPM (IMERG) technical documentation. NASA/GSFC Code 612 Tech. Doc., 48 pp., http://pmm.nasa.gov/sites/default/files/document_files/IMERG_doc.pdf.

——, and Coauthors, 2020: Integrated Multi-satellite Retrievals for the Global Precipitation Measurement (GPM) Mission (IMERG). *Satellite Precipitation Measurement*, Springer, 343–353.

Imaoka, K., and K. Nakamura, 2012: Statistical analysis of the life cycle of isolated tropical cold cloud systems using MTSAT-1R and TRMM data. *Mon. Wea. Rev.*, **140**, 3552–3572, https://doi.org/10.1175/MWR-D-11-00364.1.

Inoue, T., D. Vila, K. Rajendran, A. Hamada, X. Wu, and L. A. Machado, 2009: Life cycle of deep convective systems over the eastern tropical Pacific observed by TRMM and GOES-W. *J. Meteor. Soc. Japan*, **87A**, 381–391, https://doi.org/10.2151/jmsj.87A.381.

Janowiak, J. E., V. E. Kousky, and R. J. Joyce, 2005: Diurnal cycle of precipitation determined from the CMORPH high spatial and temporal resolution global precipitation analyses. *J. Geophys. Res.*, **110**, D23105, https://doi.org/10.1029/2005JD006156.

Jiang, H., C. Liu, and E. J. Zipser, 2011: A TRMM-based tropical cyclone cloud and precipitation feature database. *J. Appl. Meteor. Climatol.*, **50**, 1255–1274, https://doi.org/10.1175/2011JAMC2662.1.

Joyce, R. J., and P. Xie, 2011: Kalman filter–based CMORPH. *J. Hydrometeor.*, **12**, 1547–1563, https://doi.org/10.1175/JHM-D-11-022.1.

——, J. E. Janowiak, P. A. Arkin, and P. Xie, 2004: CMORPH: A method that produces global precipitation estimates from passive microwave and infrared data at high spatial and temporal resolution. *J. Hydrometeor.*, **5**, 487–503, https://doi.org/10.1175/1525-7541(2004)005<0487:CAMTPG>2.0.CO;2.

Karbalaee, N., K. Hsu, S. Sorooshian, and D. Braithwaite, 2017a: Bias adjustment of infrared-based rainfall estimation using passive microwave satellite rainfall data. *J. Geophys. Res. Atmos.*, **122**, 3859–3876, https://doi.org/10.1002/2016JD026037.

——, P. E. Kirstetter, and J. J. Gourley, 2017b: Improving precipitation estimates over the western United States using GOES-R precipitation data. *2017 Fall Meeting*, San Francisco, CA, Amer. Geophys. Union, Abstract H54F-06.

Kerns, B. W., and S. S. Chen, 2016: Large-scale precipitation tracking and the MJO over the Maritime Continent and Indo-Pacific warm pool. *J. Geophys. Res. Atmos.*, **121**, 8755–8776, https://doi.org/10.1002/2015JD024661.

——, and ——, 2020: A 20-year climatology of Madden-Julian oscillation convection: Large-scale precipitation tracking from TRMM-GPM rainfall. *J. Geophys. Res. Atmos.*, **125**, e2019JD032142, https://doi.org/10.1029/2019JD032142.

Kubota, T., and Coauthors, 2007: Global precipitation map using satellite-borne microwave radiometers by the GSMaP project: Production and validation. *IEEE Trans. Geosci. Remote Sens.*, **45**, 2259–2275, https://doi.org/10.1109/TGRS.2007.895337.

Kummerow, C. D., W. Barnes, T. Kozu, J. Shiue, and J. Simpson, 1998: The Tropical Rainfall Measuring Mission (TRMM) sensor package. *J. Atmos. Oceanic Technol.*, **15**, 809–817, https://doi.org/10.1175/1520-0426(1998)015<0809:TTRMMT>2.0.CO;2.

——, D. L. Randel, M. Kulie, N. Y. Wang, R. Ferraro, S. Joseph Munchak, and V. Petkovic, 2015: The evolution of the Goddard profiling algorithm to a fully parametric scheme. *J. Atmos. Oceanic Technol.*, **32**, 2265–2280, https://doi.org/10.1175/JTECH-D-15-0039.1.

Laing, A. G., and M. Fritsch, 1993a: Mesoscale convective complexes in Africa. *Mon. Wea. Rev.*, **121**, 2254–2263, https://doi.org/10.1175/1520-0493(1993)121<2254:MCCIA>2.0.CO;2.

——, and ——, 1993b: Mesoscale convective complexes over Indian monsoon region. *J. Climate*, **6**, 911–919, https://doi.org/10.1175/1520-0442(1993)006<0911:MCCOTI>2.0.CO;2.

Li, R., K. Wang, and D. Qi, 2018; Validating the integrated multisatellite retrievals for global precipitation measurement in terms of diurnal variability with hourly gauge observations collected at 50,000 stations in China. *J. Geophys. Res. Atmos.*, **123**, 10 423–10 442, https://doi.org/10.1029/2018JD028991.

Liu, C., E. J. Zipser, and S. W. Nesbitt, 2007: Global distribution of tropical deep convection: Different perspectives from TRMM infrared and radar data. *J. Climate*, **20**, 489–503, https://doi.org/10.1175/JCLI4023.1.

——, ——, D. J. Cecil, S. W. Nesbitt, and S. Sherwood, 2008: A cloud and precipitation feature database from nine years of TRMM observations. *J. Appl. Meteor. Climatol.*, **47**, 2712–2728, https://doi.org/10.1175/2008JAMC1890.1.

Luo, Y., H. Wang, R. Zhang, W. Qian, and Z. Luo, 2013: Comparison of rainfall characteristics and convective properties of monsoon precipitation systems over South China and the Yangtze and Huai River basin. *J. Climate*, **26**, 110–132, https://doi.org/10.1175/JCLI-D-12-00100.1.

Machado, L. A. T., and W. B. Rossow, 1993: Structural characteristics and radiative properties of tropical cloud clusters. *Mon. Wea. Rev.*, **121**, 3234–3260, https://doi.org/10.1175/1520-0493(1993)121<3234:SCARPO>2.0.CO;2.

——, and H. Laurent, 2004: The convective system area expansion over Amazonia and its relationships with convective system life duration and high-level wind divergence. *Mon. Wea. Rev.*, **132**, 714–725, https://doi.org/10.1175/1520-0493(2004)132<0714:TCSAEO>2.0.CO;2.

——, W. B. Rossow, R. L. Guedes, and A. W. Walker, 1998: Life cycle variations of mesoscale convective systems over the Americas. *Mon. Wea. Rev.*, **126**, 1630–1654, https://doi.org/10.1175/1520-0493(1998)126<1630:LCVOMC>2.0.CO;2.

Maranan, M., A. H. Fink, P. Knippertz, L. K. Amekudzi, W. A. Atiah, and M. Stengel, 2020: A process-based validation of GPM IMERG and its sources using a mesoscale rain gauge network in the West African forest zone. *J. Hydrometeor.*, **21**, 729–749, https://doi.org/10.1175/JHM-D-19-0257.1.

Marchand, R., G. G. Mace, T. Ackerman, and G. Stephens, 2008: Hydrometeor detection using *Cloudsat*—An Earth-orbiting 94-GHz cloud radar. *J. Atmos. Oceanic Technol.*, **25**, 519–533, https://doi.org/10.1175/2007JTECHA1006.1.

Martin, D. W., and A. J. Schreiner, 1981: Characteristics of West African and east Atlantic cloud clusters: A survey from GATE. *Mon. Wea. Rev.*, **109**, 1671–1688, https://doi.org/10.1175/1520-0493(1981)109<1671:COWAAE>2.0.CO;2.

Masunaga, H., 2012: A satellite study of the atmospheric forcing and response to moist convection over tropical and subtropical oceans. *J. Atmos. Sci.*, **69**, 150–167, https://doi.org/10.1175/JAS-D-11-016.1.

——, 2013: A satellite study of tropical moist convection and environmental variability: A moisture and thermal budget analysis. *J. Atmos. Sci.*, **70**, 2443–2466, https://doi.org/10.1175/JAS-D-12-0273.1.

——, M. Schröder, F. A. Furuzawa, C. Kummerow, E. Rustemeier, and U. Schneider, 2019: Inter-product biases in global precipitation extremes. *Environ. Res. Lett.*, **14**, 125016, https://doi.org/10.1088/1748-9326/ab5da9.

McAnelly, R. L., and W. R. Cotton, 1989: The precipitation life cycle of mesoscale convective complexes over the central United States. *Mon. Wea. Rev.*, **117**, 784–808, https://doi.org/10.1175/1520-0493(1989)117<0784:TPLCOM>2.0.CO;2.

Miller, D., and J. M. Fritsch, 1991: Mesoscale convective complexes in the western Pacific region. *Mon. Wea. Rev.*, **119**, 2978–2992, https://doi.org/10.1175/1520-0493(1991)119<2978:MCCITW>2.0.CO;2.

Mohr, K. I., J. S. Famiglietti, and E. J. Zipser, 1999: The contribution to tropical rainfall with respect to convective system type, size, and intensity estimated from the 85-GHz ice-scattering signature. *J. Appl. Meteor.*, **38**, 596–606, https://doi.org/10.1175/1520-0450(1999)038<0596:TCTTRW>2.0.CO;2.

Nguyen, P., and Coauthors, 2017: Evaluation of CMIP5 model precipitation using PERSIANN-CDR. *J. Hydrometeor.*, **18**, 2313–2330, https://doi.org/10.1175/JHM-D-16-0201.1.

——, M. Ombadi, S. Sorooshian, K. Hsu, A. AghaKouchak, D. Braithwaite, H. Ashouri, and A. R. Thorstensen, 2018: The PERSIANN family of global satellite precipitation data: A review and evaluation of products. *Hydrol. Earth Syst. Sci.*, **22**, 5801–5816, https://doi.org/10.5194/hess-22-5801-2018.

Rossow, W. B., and R. A. Schiffer, 1999: Advances in understanding clouds from ISCCP. *Bull. Amer. Meteor. Soc.*, **80**, 2261–2288, https://doi.org/10.1175/1520-0477(1999)080<2261:AIUCFI>2.0.CO;2.

——, A. Mekonnen, C. Pearl, and W. Goncalves, 2013: Tropical precipitation extremes. *J. Climate*, **26**, 1457–1466, https://doi.org/10.1175/JCLI-D-11-00725.1.

Rowell, D. P., and J. R. Milford, 1993: On the generation of African squall lines. *J. Climate*, **6**, 1181–1193, https://doi.org/10.1175/1520-0442(1993)006<1181:OTGOAS>2.0.CO;2.

Schumacher, C., and R. A. Houze Jr., 2003: Stratiform rain in the tropics as seen by the TRMM precipitation radar. *J. Climate*, **16**, 1739–1756, https://doi.org/10.1175/1520-0442(2003)016<1739:SRITTA>2.0.CO;2.

Sharifi, E., B. Saghafian, and R. Steinacker, 2019: Copula-based stochastic uncertainty analysis of satellite precipitation products. *J. Hydrol.*, **570**, 739–754, https://doi.org/10.1016/j.jhydrol.2019.01.035.

Sorooshian, S., K. L. Hsu, X. Gao, H. V. Gupta, B. Imam, and D. Braithwaite, 2000: Evaluation of PERSIANN system satellite-based estimates of tropical rainfall. *Bull. Amer. Meteor. Soc.*, **81**, 2035–2046, https://doi.org/10.1175/1520-0477(2000)081<2035:EOPSSE>2.3.CO;2.

——, X. Gao, K. Hsu, R. A. Maddox, Y. Hong, H. V. Gupta, and B. Imam, 2002: Diurnal variability of tropical rainfall retrieved from combined GOES and TRMM satellite information. *J. Climate*, **15**, 983–1001, https://doi.org/10.1175/1520-0442(2002)015<0983:DVOTRR>2.0.CO;2.

Stephens, G. L., and Coauthors, 2008: CloudSat mission: Performance and early science after the first year of operation. *J. Geophys. Res.*, **113**, D00A18, https://doi.org/10.1029/2008JD009982.

Takahashi, H., and Z. J. Luo, 2014: Characterizing tropical over-shooting deep convection from joint analysis of CloudSat and geostationary satellite observations. *J. Geophys. Res. Atmos.*, **119**, 112–121, https://doi.org/10.1002/2013JD020972.

Tan, J., G. J. Huffman, D. T. Bolvin, and E. J. Nelkin, 2019: Diurnal cycle of IMERG V06 precipitation. *Geophys. Res. Lett.*, **46**, 13 584–13 592, https://doi.org/10.1029/2019GL085395.

Tang, G., M. P. Clark, S. M. Papalexiou, Z. Ma, and Y. Hong, 2020: Have satellite precipitation products improved over last two decades? A comprehensive comparison of GPM IMERG with nine satellite and reanalysis datasets. *Remote Sens. Environ.*, **240**, 111697, https://doi.org/10.1016/j.rse.2020.111697.

Tao, W. K., T. Iguchi, and S. Lang, 2019: Expanding the Goddard CSH algorithm for GPM: New extratropical retrievals. *J. Appl. Meteor. Climatol.*, **58**, 921–946, https://doi.org/10.1175/JAMC-D-18-0215.1.

Tian, F., S. Hou, L. Yang, H. Hu, and A. Hou, 2018: How does the evaluation of the GPM IMERG rainfall product depend on gauge density and rainfall intensity? *J. Hydrometeor.*, **19**, 339–349, https://doi.org/10.1175/JHM-D-17-0161.1.

Ushio, T., and Coauthors, 2009: A Kalman filter approach to the Global Satellite Mapping of Precipitation (GSMaP) from combined passive microwave and infrared radiometric data. *J. Meteor. Soc. Japan*, **87A**, 137–151, https://doi.org/10.2151/jmsj.87A.137.

Vant-Hull, B., W. Rossow, and C. Pearl, 2016: Global comparisons of regional life cycle properties and motion of multiday convective systems: Tropical and midlatitude land and ocean. *J. Climate*, **29**, 5837–5858, https://doi.org/10.1175/JCLI-D-15-0698.1.

Velasco, I., and J. M. Fritsch, 1987: Mesoscale convective complexes in the Americas. *J. Geophys. Res.*, **92**, 9591–9613, https://doi.org/10.1029/JD092iD08p09591.

Wang, H., L. Wang, J. He, F. Ge, Q. Chen, S. Tang, and S. Yao, 2020: Can the GPM IMERG hourly products replicate the variation in precipitation during the wet season over the Sichuan Basin, China? *Earth Space Sci.*, **7**, e2020EA001090, https://doi.org/10.1029/2020EA001090.

White, R. H., D. S. Battisti, and G. Skok, 2017: Tracking precipitation events in time and space in gridded observational data. *Geophys. Res. Lett.*, **44**, 8637–8646, https://doi.org/10.1002/2017GL074011.

Williams, M., and R. A. Houze, 1987: Satellite-observed characteristics of winter monsoon cloud clusters. *Mon. Wea. Rev.*, **115**, 505–519, https://doi.org/10.1175/1520-0493(1987)115<0505:SOCOWM>2.0.CO;2.

Woodley, W. L., C. G. Griffith, J. S. Griffin, and S. C. Stromatt, 1980: The inference of GATE convective rainfall from SMS-1 imagery. *J. Appl. Meteor.*, **19**, 388–408, https://doi.org/10.1175/1520-0450(1980)019<0388:TIOGCR>2.0.CO;2.

Xu, W., and E. J. Zipser, 2011: Diurnal variations of precipitation, deep convection, and lightning over and east of the eastern Tibetan Plateau. *J. Climate*, **24**, 448–465, https://doi.org/10.1175/2010JCLI3719.1.

Young, A. H., K. R. Knapp, A. Inamdar, W. Hankins, and W. B. Rossow, 2018: The International Satellite Cloud Climatology Project H-series climate data record product. *Earth Syst. Sci. Data*, **10**, 583–593, https://doi.org/10.5194/essd-10-583-2018.

Yuter, S. E., and R. A. Houze Jr., 1995: Three-dimensional kinematic and microphysical evolution of Florida cumulonimbus. Part II: Frequency distributions of vertical velocity, reflectivity, and differential reflectivity. *Mon. Wea. Rev.*, **123**, 1941–1963, https://doi.org/10.1175/1520-0493(1995)123<1941:TDKAME>2.0.CO;2.

Zhang, X., and E. N. Anagnostou, 2019: Evaluation of numerical weather model–based satellite precipitation adjustment in tropical mountainous regions. *J. Hydrometeor.*, **20**, 431–445, https://doi.org/10.1175/JHM-D-18-0008.1.

Zhou, Y., K. Nelson, K. I. Mohr, G. J. Huffman, R. Levy, and M. Grecu, 2019: A spatial-temporal extreme precipitation database from GPM IMERG. *J. Geophys. Res. Atmos.*, **124**, 10 344–10 363, https://doi.org/10.1029/2019JD030449.